UNIVERSITÀ DEGLI STUDI DI PADOVA

DIPARTIMENTO DI FISICA E ASTRONOMIA
"GALILEO GALILEI"

Corso di Laurea Triennale in Fisica

SVILUPPO DI UNA DIAGNOSTICA PER MISURARE LA CARICA SPAZIALE DI UN FASCIO DI IONI NEGATIVI

DEVELOPMENT OF AN INSTRUMENT TO MEASURE SPACE CHARGE COMPENSATION IN NEGATIVE ION BEAMS

Laureando
Gabriele Carozzi

Relatore
Dott. Gianluigi Serianni

Correlatore
Dott. Emanuele Sartori

ANNO ACCADEMICO 2015/2016

Sommario

Le misure del potenziale di plasma e dello spettro di energia delle particelle secondarie nella regione di deriva di un fascio di ioni negativi danno informazioni sulla formazione di plasma indotta dal fascio e sul trasporto del fascio stesso attraverso gas a bassa pressione. La formazione di plasma in sistemi di fasci di ioni negativi e le caratteristiche di tale plasma sono utili specialmente nell'analisi della compensazione di carica spaziale, che ha un importante impatto sullo studio di fasci di particelle neutre utilizzati per scaldare il plasma all'interno di un tokamak.
Dopo una breve introduzione sulle sorgenti di ioni negativi e sulla compensazione di carica spaziale, viene fatta un'analisi dettagliata di quest'ultima. I risultati vengono utilizzati per sviluppare una simulazione numerica e per progettare e costruire una sonda a potenziale ritardante per lo studio della compensazione di carica spaziale. Dopo la costruzione, la sonda viene testata in un dispositivo magnetron per sputtering. I risultati del test sono ottimi: molto insegnano sul funzionamento della sonda e inoltre suggeriscono come continuare il lavoro futuro.

Abstract

The measurement of the plasma potential and the energy spectrum of secondary particles in the drift region of a negative ion beam offers an insight into beam-induced plasma formation and beam transport in low pressure gases. Plasma formation in negative ion beam systems and the characteristics of such plasma are relevant especially for space charge compensation, which has an important role in the studies for neutral beam injector systems for plasma heating in a tokamak.
After a brief introduction on negative ion sources and space charge compensation, a detailed analysis of the latter is made. Results are used to develop a numerical simulation and to design and build a retarding field energy analyzer to study space charge compensation. After construction, the analyzer is tested inside a magnetron sputtering device. Test results are successful: they show how to operate the analyzer and also suggest how future work should be done.

Contents

Chapter 1

Introduction

The study of negative ion sources has seen a huge increase in the past few decades, caused by their wide variety of application in different fields.
One of the main fields of application is nuclear fusion: negative ion beams are used in neutral beam injection systems to accelerate ions which are then neutralized and used to heat plasma in a tokamak. NIO1 (Negative Ion Optimization phase 1) is an example of a negative ion source and accelerator that has been built and is currently operational at Consorzio RFX in Padova [1] [2].
Other applications are acceleration systems used in particle physics experiments: an example of this is Linac4, a project currently being developed at CERN to upgrade the injector chain of the Large Hadron Collider [3].
Lastly, negative ion beams are relevant in the medical field: they are used in charged-particle radiotherapy and in the production of isotopes for radionuclide imaging with positron emission tomography [4].

One of the main concerns when working with negative ion sources is beam collimation during transport. Particles that make up the beam all have the same electric charge, therefore they tend to repel each other: this causes the beam to widen after being accelerated. In environments where the beam needs to travel long distances before reaching its target, this effect is detrimental and needs to be taken care of. This is where space charge compensation plays its role.

1.1 Space charge compensation

If the beam travels in absolute vacuum, the beam widens as described above. However, if low pressure background gas is present, collision of beam particles with this gas can create ionized pairs of positive ions and electrons. Electrons, due to their higher mobility and the negative potential caused by the beam, tend to move away from the beam, while positive ions remain trapped in the potential well. Over time, positive ions compensate for the negative beam charge and the potential rises, but this effect does not stop when zero is reached: it is commonly found that at equilibrium the potential is overcompensated and thus it is slightly positive [5] (Fig. 1.1). The positive potential that is created this way allows beam particles to remain close to each other, thus allowing the beam

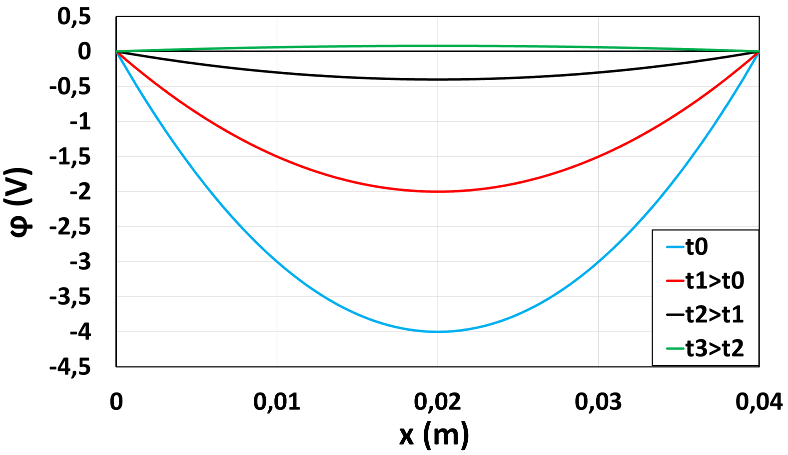

Figure 1.1: Example of space charge compensation over time in a negative ion beam.

to travel further. All this implies that a deep understanding of space charge compensation is fundamental when operating negative ion sources, and being able to measure the overcompensated potential allows researchers to find more efficient configurations of the device.

In order to make this kind of measurements, two main techniques are used: one is based on electron beam probing, the other on a retarding field energy analyzer.

Electron beam probing

Electron beam probing consists in using an electron gun to create a monochromatic electron beam. Electrons are sent through the main beam, perpendicular to its axis, and are collected on the other side. By measuring the deflection of the electron beam and repeating this operation at various angles and distances from the main beam axis, it is possible to reconstruct the potential profile by applying tomography techniques [6].

Retarding field energy analyzer

A retarding field energy analyzer consists in a conductive case located so that it views the beam perpendicularly. It works by first filtering out electrons and negative ions: remaining positive ions expelled from the beam due to the slightly positive potential can enter the analyzer and reach the collector at the opposite end. Inside the analyzer, a grid with varying potential is employed to filter positive ions: only those with sufficient energy can go past it. By scanning over the retarding grid potential, it is possible to obtain the ion energy distribution function (IEDF) [7].

1.2 Thesis motivation

NIO1 is currently being used to investigate the optimal configurations for negative ion beam production. Space charge compensation plays a key role, so gaining a deep understanding of this effect and being able to control it is very important.

The purpose of this thesis is to study the phenomena that cause space charge compensation inside NIO1. This analysis is then used to develop a retarding field energy analyzer, build it and then test its operation. At the same time, a numerical simulation is also developed to create a model of space charge compensation mechanisms.

The diagnostic developed with this thesis is currently being installed to study space charge compensation in the negative ion beam used at the National institute for Fusion Science (NIFS) in Toki, Japan.

Chapter 2

Analysis of space charge compensation

The first step to understand space charge compensation is to evaluate the interaction of the beam with the background gas: this means studying what types of particles are created and what their velocity distribution is. After this, it is also important to estimate how these particles interact with each other and how these interactions can affect the current collected by the energy analyzer: if it were too low, the measurement complexity might compromise the entire work.

Values used in numerical examples stem from the typical operational conditions of the negative ion beam used at the National Institute for Fusion Science (NIFS) in Toki, Japan [8]: beam energy is 60 keV, with a current of 250 mA. Calculations are also made for one of the configurations of the negative ion beam NIO1 [2] used at the RFX facility in Padova: beam energy is 5 keV with a current of 600 μA.
Cross sections are taken from Barnett [9].

2.1 Beam composition

Initially the beam only contains negative ions H^-, but after traveling through the background gas the population of particles changes. In collisions these ions can lose one or more electrons, thus creating H^0 and H^+:

$$\underline{H}^- + H_2 \rightarrow \underline{H}^0 + H_2 + e \qquad (2.1)$$

$$\underline{H}^- + H_2 \rightarrow \underline{H}^+ + H_2 + 2e \qquad (2.2)$$

$$\underline{H}^0 + H_2 \rightarrow \underline{H}^+ + H_2 + e \qquad (2.3)$$

$$\underline{H}^+ + H_2 \rightarrow \underline{H}^0 + H_2^+ \qquad (2.4)$$

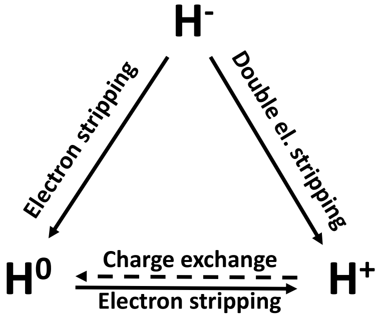

The neutral particles and the positive ions still move parallel to the beam axis and mostly retain the energy of the negative ions they originated from, whereas electrons are emitted with the same velocity as the ions, parallel to the beam axis. This means that the electron energy will be much lower:

$$E_e = \frac{m_e}{m_i} E_i \tag{2.5}$$

Flux change for each species inside the beam will be:

$$H^- : \quad d\Gamma^- = -\Gamma^- n(\sigma_{-0} + \sigma_{-+})\, dx \tag{2.6}$$
$$H^0 : \quad d\Gamma^0 = \Gamma^- n\sigma_{-0}\, dx - \Gamma^0 n\sigma_{0+}\, dx + \Gamma^+ n\sigma_{+0}\, dx \tag{2.7}$$
$$H^+ : \quad \frac{\Gamma^+}{\Gamma_0^-} = 1 - \frac{\Gamma^-}{\Gamma_0^-} - \frac{\Gamma^0}{\Gamma_0^-} \tag{2.8}$$

where Γ_0^- is the initial flux of H^-.
Calculations are made for a 60 keV H^- beam going through a region filled with H_2 at various pressures (Fig. 2.1 shows an example at 0.003 Pa). Cross sections are:

- $H^- \rightarrow H^0 \quad \sigma_{-0} = 5.5 \cdot 10^{-20}$ m^2
- $H^- \rightarrow H^+ \quad \sigma_{-+} = 3.6 \cdot 10^{-21}$ m^2
- $H^0 \rightarrow H^+ \quad \sigma_{0+} = 1.2 \cdot 10^{-20}$ m^2
- $H^+ \rightarrow H^0 \quad \sigma_{+0} = 1.4 \cdot 10^{-20}$ m^2

Results for the 60 keV beam at a distance $x = 1$ m from the source are shown in table 2.1.

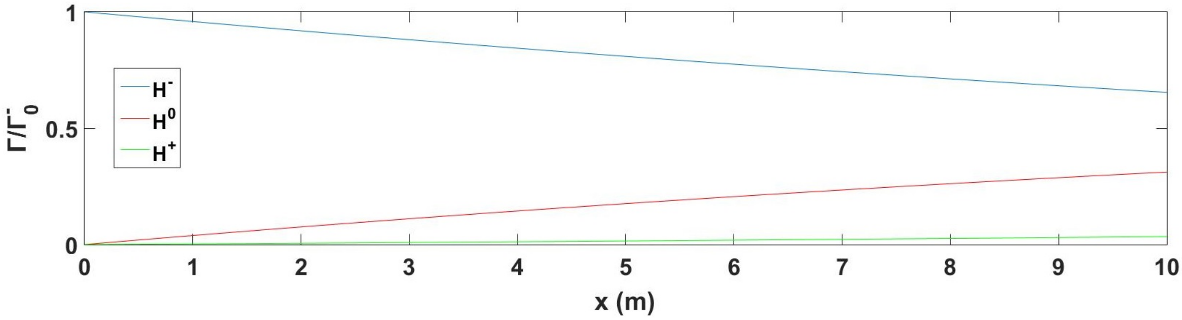

Figure 2.1: Changes in beam composition with distance. E_{beam} = 60 keV, background gas H_2, pressure 0.003 Pa.

Pressure	Γ^-/Γ_0^-	Γ^0/Γ_0^-	Γ^+/Γ_0^-
0.3	1.44%	62.97%	35.59%
0.03	65.4%	31.16%	3.44%
0.003	95.84%	3.89%	0.27%
0.0003	99.58%	0.40%	0.02%

Table 2.1

A similar calculation is also made for a 5 keV H^- beam going through a region filled with H_2 at 0.165 Pa (Fig. 2.2).

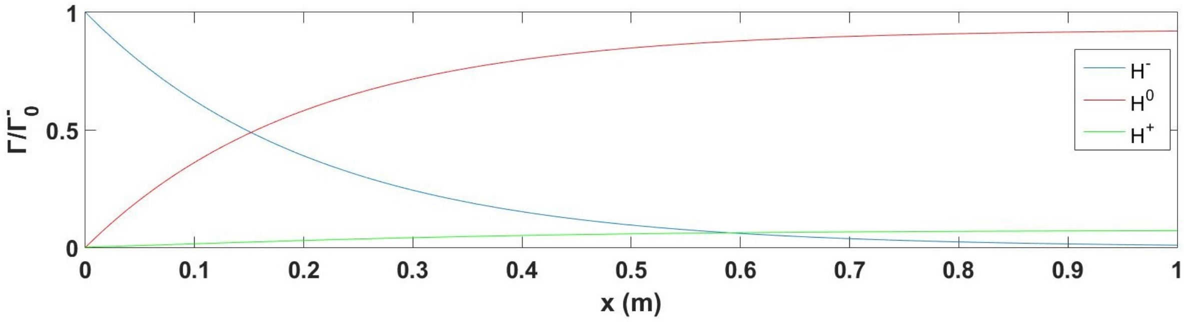

Figure 2.2: Changes in beam composition with distance. $E_{beam} = 5$ keV, background gas H_2, pressure 0.165 Pa.

2.2 Background gas ionization

Beam particles collide with background gas, causing ionization.
The creation rate of charges from ionization is given by

$$S = n_t \sigma \Gamma_p \tag{2.9}$$

where

- S is the local source term (number of generated particles per unit time and volume);
- n_t is the numeric density of target (background gas) particles;
- σ is the collision cross section;
- Γ_p is the flux of projectile (moving) particles.

Since the beam contains several different types of particles all colliding with the background gas, total local source term can be computed as

$$S_{tot} = n_{bg} \sigma_{eff} \Gamma_{beam} \tag{2.10}$$

$$\sigma_{eff} = \sum_i \frac{\Gamma_i}{\Gamma_{beam}} \sigma_i \tag{2.11}$$

where the index i represents every single type of particles inside the beam.
To calculate S_{tot} it is necessary to know how beam particles interact with background gas.

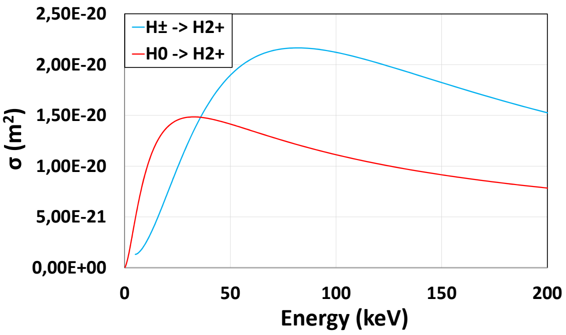

Figure 2.3: Cross sections for beam induced ionization.

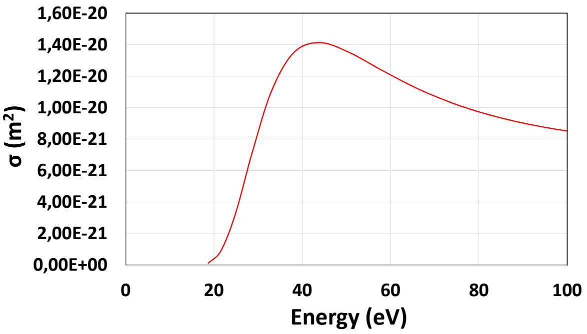

Figure 2.4: Cross section for electron induced ionization.

2.2.1 Beam induced ionization

As stated earlier, $H^{\pm}$ and H^0 inside the beam mostly retain the beam energy. When they collide with background gas they can ionize it, thus creating H_2^+ ions (which will be referred to as "secondary ions"). The interactions are:

$$\underline{H}^+ + H_2 \rightarrow \underline{H}^+ + H_2^+ + e \tag{2.12}$$

$$\underline{H}^- + H_2 \rightarrow \underline{H}^- + H_2^+ + e \tag{2.13}$$

$$\underline{H}^0 + H_2 \rightarrow \underline{H}^0 + H_2^+ + e \tag{2.14}$$

Cross section values can be seen in Fig. 2.3. The same cross section is used when the projectiles are H^+ and H^-. At $E = 60$ keV, cross section values are $\sigma_{\pm} = 2.05 \cdot 10^{-20}$ m^2 and $\sigma_0 = 1.35 \cdot 10^{-20}$ m^2.

2.2.2 Stripped electrons

As seen earlier, (2.1), (2.2) and (2.3) also give electrons that move parallel to the beam axis, with the same velocity as the more massive particles inside the beam. This means that their energy will be small (see (2.5)), but it can still be enough to further ionize background gas. The interaction is:

$$e + H_2 \rightarrow e + H_2^+ + e \tag{2.15}$$

Cross section values can be seen in Fig. 2.4. For a 60 keV beam, (2.5) gives $E_e = 32.7$ eV; the cross section is $\sigma_e = 1.07 \cdot 10^{-20}$ m^2. In the 5 keV beam, stripped electrons energy is too low to cause further ionization: in this case, $\sigma_e = 0$ m^2.

2.2.3 Plasma electrons

The energy of electrons generated during background gas ionization is never higher than 10 eV with a 60 keV beam, and even lower with a 5 keV beam. Since the lower threshold for electron induced ionization is 16 eV [10], these electrons can never cause additional ionization.

2.2.4 Effective cross section

At this point, a calculation of σ_{eff} is possible using (2.11) and data from the previous sections of this chapter.
One needs to note that the for every H^+ created by the beam two electrons are emitted, and for every H^0 one electron is emitted. Therefore (2.11) becomes:

$$\sigma_{eff} = \frac{\Gamma^- \sigma_- + \Gamma^0 \sigma_0 + \Gamma^+ \sigma_+ + (\Gamma^0 + 2\Gamma^+ + \Gamma_{H^+ \to H^0})\,\sigma_e}{\Gamma_0^-} \tag{2.16}$$

Results at distance $x = 1$ m for the 60 keV beam are shown in table 2.2. Examples of how σ_{eff} changes with distance are shown in Fig. 2.5 for the 60 keV beam and in Fig. 2.6 for the 5 keV beam.

Pressure	σ_{eff}
0.3	$3.26 \cdot 10^{-20}$
0.03	$2.24 \cdot 10^{-20}$
0.003	$2.07 \cdot 10^{-20}$
0.0003	$2.05 \cdot 10^{-20}$

Table 2.2

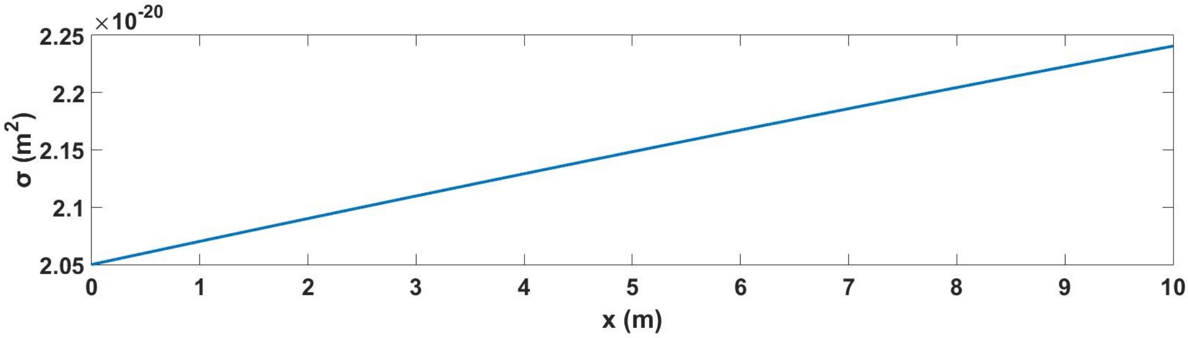

Figure 2.5: Effective cross section as a function of distance. $E_{beam} = 60$ keV, background gas H_2, pressure 0.003 Pa.

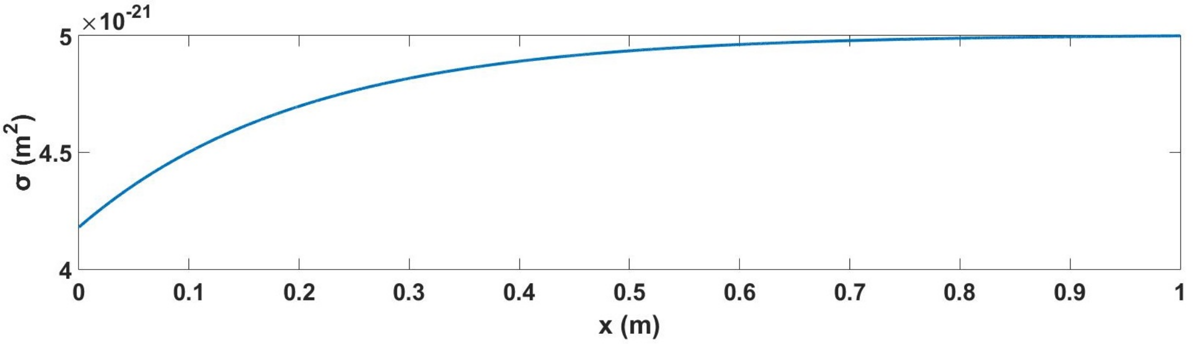

Figure 2.6: Effective cross section as a function of distance. $E_{beam} = 5$ keV, background gas H_2, pressure 0.165 Pa.

2.3 Loss of secondary ions flux due to collisions

The H_2^+ ions described above move away from the beam due to the compensating positive electric potential and are subject to collisions mainly with electrons. Other collisions are neglected due to the low expected energy of ions (around 1-1.5 eV kinetic plus potential).

Flux loss due to collisions is

$$d\Gamma = -\Gamma n \sigma \, dx \tag{2.17}$$

where n is the target numeric density (H_2^+), σ is the collision cross section and x is the distance traveled. Therefore

$$\Gamma(x) = \Gamma_0 \exp(-n\sigma x) = \Gamma_0 \exp(-\frac{x}{\lambda}) \tag{2.18}$$

with $\lambda = 1/n\sigma$ being the mean free path.

The main interaction that leads to the loss of positively charged particles is dissociative recombination, caused by the collision of electrons with secondary ions:

$$e + H_2^+ \rightarrow H + H$$

With electron energy typically ranging from 1 eV to 20 eV, the cross section for this interaction (Fig. 2.7) goes from $3.0 \cdot 10^{-21}$ m^2 to $7.2 \cdot 10^{-20}$ m^2.

The numeric density of secondary ions is expected to be around 10^{18} m^2 in the beam region and to decrease while moving away from it. If that value is considered constant, thus overestimating the number of collision in the whole region, the mean free path ranges from 13.9 m to 333.3 m. Considering that the device will be placed at a distance $d = 0.1$ m, this means that the fraction of particles lost due to this interaction goes from 0.03% in the best case, rising up to 0.72% in the worst case.

This suggests that these collisions have a really small impact on the current that will eventually be collected, which is a positive result.

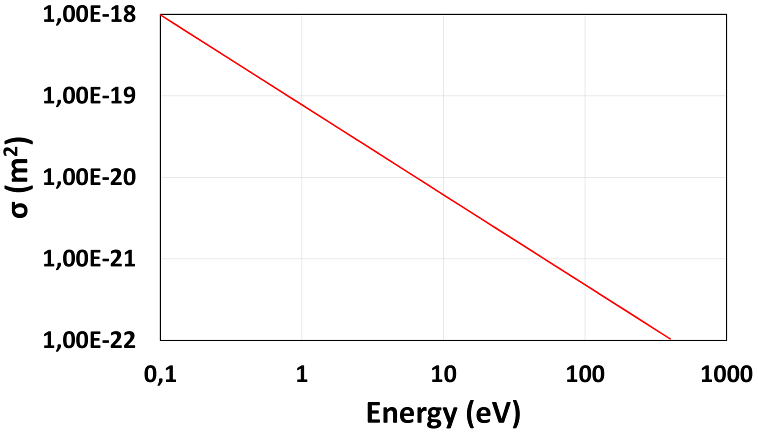

Figure 2.7: Cross section for dissociative recombination.

2.4 Estimate of particle flux

With these first results it is possible to make an initial very rough estimate of how much positive ion current can be collected. While not being precise, it can still give important information on the feasibility of the analyzer.
It is assumed that the beam only contains H^- ions with uniform density; it can be approximated as a cylinder with radius $R = 0.005$ m. It is also assumed that all secondary ions created by the beam colliding with the background gas are expelled radially. Background gas is molecular hydrogen H_2 at temperature $T = 300$ K and pressure $P = 0.01$ Pa.
The number of particles generated per unit time and volume has already been calculated in (2.9). Therefore the number of particles generated per unit time is

$$\frac{N}{\Delta t} = n_{bg}\sigma \Gamma_{beam}\pi R^2 \Delta z = n_{bg}\sigma \Delta z \frac{I_{beam}}{e} \tag{2.19}$$

where Δz is a length along the beam axis and I_{beam} is the beam current.
Since it has been established that positive ion loss is negligible in the region studied, at equilibrium the flux of secondary ions through the lateral surface of a cylinder with axis coincident with the beam axis, radius d and height Δz is

$$\Gamma(d) = \frac{N}{\Delta t}\frac{1}{2\pi d \Delta z} \tag{2.20}$$

and the total current collected by the analyzer is

$$I = e\Gamma(d)A \tag{2.21}$$

where A is the area of the collection surface.
Using (2.21) and the values $n_{bg} = 7.25 \cdot 10^{17}$ m^{-3} (pressure 0.003 Pa), $\sigma = 2.07 \cdot 10^{-20}$ m^2

(calculated earlier as σ_{eff}), $I_{beam} = 0.25$ A, $d = 0.1$ m, $A = 5{\cdot}10^{-3}$ m^2 (circular with radius $r = 0.04$ m) the total collected current is $I = 2.98 \cdot 10^{-5}$ A, which is easily measurable with a multimeter and a 100 kΩ resistance. These results support the feasibility of a measurement using a retarding field energy analyzer.

2.5 Estimate of particle energy distribution

In order to observe the energy spectrum of secondary ions it is necessary to study the number of collected ions as a function of their energy. In order to do so, a simple numeric simulation was developed.

It is assumed that the the system follows cylindrical symmetry: only the radial coordinate is considered, thus ignoring axial and azimuthal directions. In the simulation, the beam numeric density is parabolic:

$$n(r) = \begin{cases} n_0\left(1 - \left(\frac{r}{R}\right)^2\right) & 0 \le r \le R \\ 0 & r > R \end{cases} \tag{2.22}$$

The electric potential profile is also assumed parabolic:

$$V(r) = \begin{cases} V_0\left(1 - \left(\frac{r}{L}\right)^2\right) & 0 \le r \le L \\ 0 & r > L \end{cases} \tag{2.23}$$

This assumption is not an accurate model of the real profile, but is enough to understand how the electric potential will affect the shape of the signal collected by the analyzer.

When particles are created, they are given a potential energy and a kinetic energy.
The kinetic energy is calculated by giving the particle velocity sampled from a one-dimensional Maxwell-Boltzmann distribution with temperature T:

$$f(v) = \left(\frac{m}{2\pi k_B T}\right)^{1/2} e^{-mv^2/2k_BT} \tag{2.24}$$

$$v = \sqrt{\frac{k_B T}{2m}}\sqrt{-2\ln u_1}\cos(2\pi u_2) \tag{2.25}$$

where u_1 and u_2 are independent random numbers: u_1 generated from a uniform distribution in $]0,1]$ and u_2 generated from a uniform distribution in $[0,1]$. When a particle is generated with negative velocity (moving towards the beam center) it counts as if it were moving in the opposite direction: due to the large number of particles generated, for every particle moving towards the beam center that is "lost" another one coming from the opposite side is expected to be "gained".
To calculate the potential energy, it is necessary to know the position where the particle is generated, which is sampled from a probability density function (pdf). Background gas density and cross section are constant relative to the radial coordinate, so (2.9) varies with

r only due to $\Gamma_{beam}(r) = n_{beam}(r)v_{beam}$. Therefore the pdf is obtained by re-normalizing (2.22) so that

$$2\pi \int_0^{+\infty} n(r)rdr = 1 \tag{2.26}$$

which gives the pdf

$$f(r) = \frac{2}{\pi R^2}\left(1 - \left(\frac{r}{R}\right)^2\right) \qquad r \in \,]0, R] \tag{2.27}$$

with cumulative distribution function (CDF)

$$F(r) = 1 - \frac{\left(r^2 - R^2\right)^2}{R^4} \qquad r \in \,]0, R] \tag{2.28}$$

By inverting it the randomly generated position is obtained:

$$r = R\sqrt{1 - \sqrt{1 - u}} \tag{2.29}$$

where u is generated randomly from a uniform distribution in $[0, 1]$. The potential energy is then calculated by using (2.29) in (2.23).

Every time the simulation runs, the following operations are performed:

1. L, T, R are set by the user;
2. 10^6 secondary ions are generated with energy described above;
3. Maximum and minimum energy values are calculated and the interval is split into 10^5 bins, each with its own energy level; since the energy of each particle is sampled from a distribution, maximum and minimum values may change slightly between simulation runs, therefore they are calculated each time by finding the two particles with the highest and lowest energy;
4. For every bin, all particles are checked: if their energy is higher than that of the bin, the bin counter increases;
5. The results are printed in a .csv file.

Results are shown in Fig. 2.8 and Fig. 2.9. What can be noted is how differently curves reach $N/N_{tot} = 1$. When $L = R$, particles are generated with a wide spectrum of potential energy, comparable to that of thermal energy (Fig. 2.8), the curve smoothly reaches its maximum. Instead, when potential energy spectrum is much tighter (Fig. 2.9), the curve sharply reaches its maximum. From this it is possible to deduce that the high energy tail is only due to the thermal distribution of the velocity of particles, while the comparison of an inflection point and the smooth trend towards the maximum is caused by a wider spectrum of potential energy with which particles are generated.

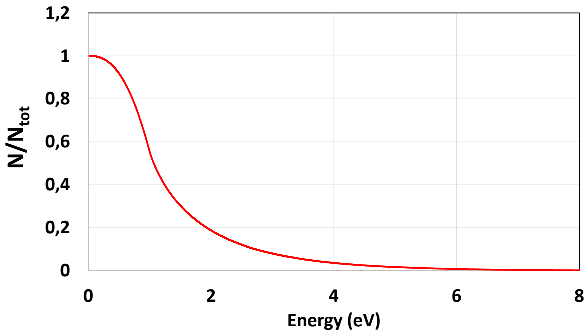

Figure 2.8: Fraction of particles vs. energy ($R = 5$ mm, $L = 5$ mm, $V_0 = 1$ V, $T = 1.5$ eV).

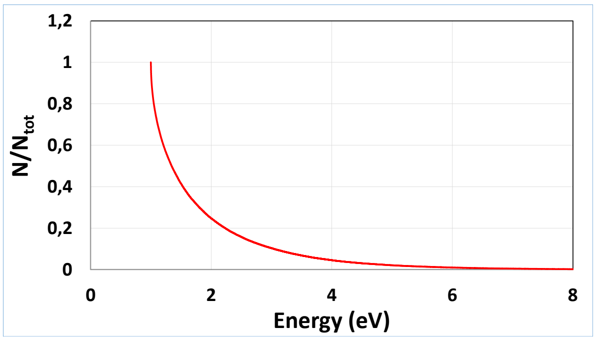

Figure 2.9: Fraction of particles vs. energy ($R = 5$ mm, $L = 10$ cm, $V_0 = 1$ V, $T = 1.5$ eV).

Chapter 3

Design and development of the 4-Grid energy analyzer

The basic idea for the structure of the analyzer (Fig. 3.1) involves four conductive grids in front of a collector. The grids are separated by a layer of insulating material to avoid contact with each other. All the grids are located inside a conductive case but do not come into contact with it, except for the grid that covers the entrance. The case potential V_{case} can be either grounded, left floating or set by a power supply.

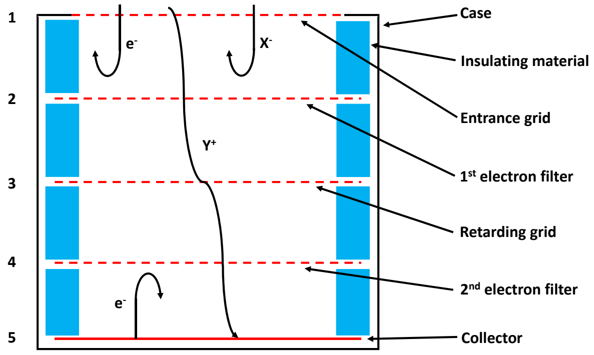

Figure 3.1: Energy analyzer schematic.

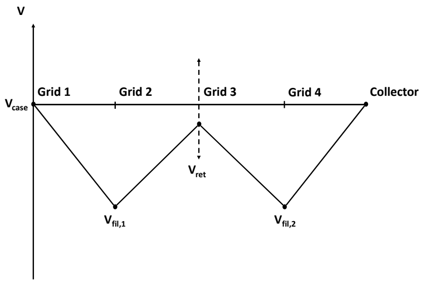

Figure 3.2: Configuration of the electric potential in the energy analyzer

1. Entrance of the analyzer: it is short-circuited with the entire case;
2. First electron filter: it is negatively biased at $V_{fil,1}$ to reflect any electron or negative ion that may come from outside;
3. Retarding grid: its potential V_{ret} is variable and is used to filter secondary ions based on their energy;
4. Second electron filter: secondary emission from a surface can be induced by ion impact. A flux of such electrons leaving the collector can alter the measured current, therefore they are reflected back by this second electron filter biased at $V_{fil,2}$;

5. Collector: it collects a flux of charges and is kept at the same potential as the external case, to which it is connected through a current measurement circuit.

3.1 Particle behavior inside the analyzer

Not all particles crossing the entrance grid reach the collector. Most of them collide with the grids (due to their low transparency) and the side wall inside. In these collisions the particles can either be lost or induce secondary electron emission; a fraction of these electrons can have high enough energy to reach the collector.

3.1.1 Grid transparency

The plasma the analyzer is facing must not be allowed past the entrance grid, otherwise it might disturb the measurement. In order to do so, proper mesh size for the entrance grid must be chosen. The gap between the wires must be comparable to the Debye length

$$\lambda_D = \sqrt{\frac{\varepsilon_0 k_B T_e}{n_e e^2}} \tag{3.1}$$

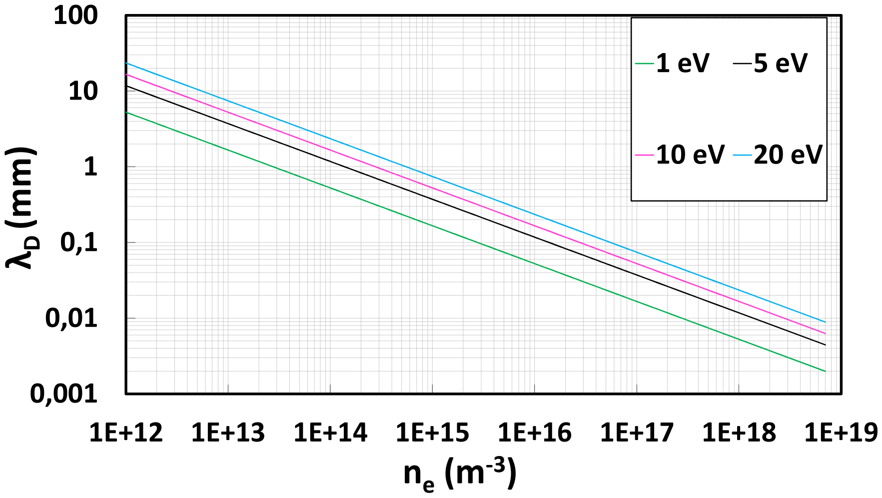

Figure 3.3: Debye length as a function of electron density.

The grids are made by metallic wire cloths, which are typically classified by distance between wires w_w and wire diameter d_w. Generally speaking, only a fraction of a woven mesh surface is open and transparent, and the geometric transparency γ is given by

$$\gamma = \frac{(w_w - d_w)^2}{w_w^2} \tag{3.2}$$

The geometric transparency γ is a first estimate of the probability that a particle crosses the mesh, instead of hitting its wires. If a single grid has transparency γ and $\mathit{\Gamma}_0$ is the flux of particles before the entrance grid, then the flux of particles reaching the collector is

$$\mathit{\Gamma}_{coll} = \gamma^4 \mathit{\Gamma}_0 \tag{3.3}$$

Expected values for λ_D (Fig. 3.3) are between 1 mm and 0.2 mm. Based on this three sets of grids have been built, as seen in table 3.1.

Aperture (mm)	Wire diameter (mm)	γ
1.7	0.28	73.7%
0.207	0.14	35.6%
0.099	0.028	60.7%

Table 3.1

3.1.2 Side wall collisions

When particles enter the analyzer, their velocity has two components: one parallel to the axis of the analyzer, $v_{\parallel}$, and one perpendicular to this axis, $\vec{v}_{\perp}$. Since the electric field is parallel to the axis and uniform in between each pair of grids, $v_{\parallel}$ changes with uniform acceleration while the particle moves towards the collector, but $\vec{v}_{\perp}$ remains constant. This means that the trajectory of particles entering the analyzer is segmented into four by the grids, and in each gap the trajectory is an arc of a parabola. This is the solution of the equation of motion of a charge in a constant electric field. the time taken to travel from grid i to grid $i+1$ is

$$t_{i,i+1} = \sqrt{\left(\frac{mv_{i\parallel}}{eE_{i,i+1}}\right) + \frac{2md}{eE_{i,i+1}}} - \frac{mv_{i\parallel}}{eE_{i,i+1}} \tag{3.4}$$

where:

- d is the distance between two adjacent grids (equal in each section);
- $E_{i,i+1} = \dfrac{V_i - V_{i+1}}{d}$ is the electric field between grids i and $i+1$;
- $v_{i\parallel} = v_{i-1\parallel} + \dfrac{eE_{i-1,i}}{m} t_{i-1,i}, \quad v_{1\parallel} = v_{\parallel}$ is the component of the particle velocity parallel to the axis at grid i.

The total time taken for a particle to travel from the entrance to the collector is then $t_{coll} = t_{1,2} + t_{2,3} + t_{3,4} + t_{4,5}$, whereas t_{loss} is the time taken for the particle to hit a side wall (it depends on the position where the particle enters the analyzer and on the direction of $v_{\perp}$), then if $t_{coll} \leq t_{loss}$ the particle is collected, otherwise it is lost.

The entrance and the collector are both circles with equal radius r. If one considers a uniformly distributed flux of particles entering the analyzer, all with the same velocity

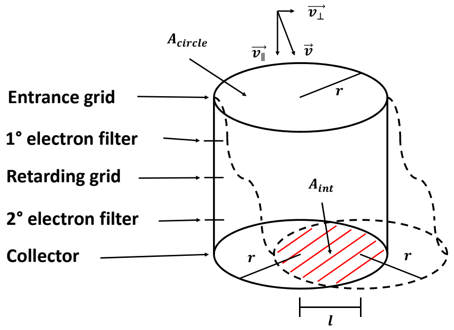

Figure 3.4: Particles shift towards the wall while moving towards the collector.

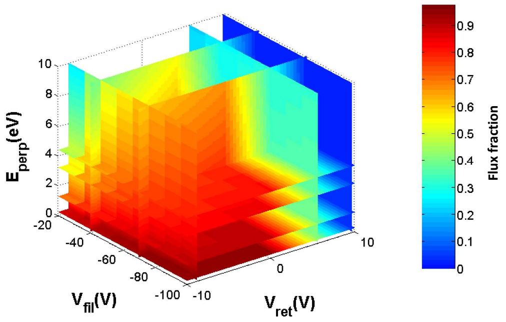

Figure 3.5: Flux fraction that reaches the collector as a function of V_{fil}, V_{ret} and $E_\perp$. A summation is made for values of $E_\parallel$ ranging from 0 to 10 eV.

components $v_\parallel$ and $\vec{v}_\perp$, by the time they reach the collector they will have traveled a distance

$$l = v_\perp t_{coll} \tag{3.5}$$

all in the same direction and part of them will be lost on the side wall. If $l < 2r$ (otherwise every particle is lost) the fraction collected is the ratio between the area of the intersection of two circles with radius r whose centers are separated by a distance l and the area of a circle with radius r (Fig. 3.4):

$$\frac{N_{coll}}{N_0} = \frac{A_{int}}{A_{circle}} = \frac{2r^2 \arccos\left(\frac{l}{2r}\right) - l\sqrt{r^2 - \frac{l^2}{4}}}{\pi r^2} \tag{3.6}$$

Equations (3.4) and (3.5) show that the total time taken for the particle to reach the collector depends on $V_{fil,1} = V_{fil,2} = V_{fil}$, V_{ret} (the entrance and the collector are at a fixed potential) and on the initial particle velocities $v_\parallel$ and $\vec{v}_\perp$. In order to understand how many particles are lost on the side wall, a scan over these parameters is made (Fig. 3.5). The most important thing to note is the dependence of total flux collected from V_{fil}: the lower it is, the higher the fraction that reaches the collector. This will especially be useful when operating the analyzer.

3.1.3 Secondary emission

Given the grids limited transparency, the particle flux is larger at the first two grids, and consequently most of secondary emission electrons generated inside the analyzer and possibly reaching the collector are produced there. Electrons produced at the entrance grid only have kinetic energy, which is not enough to go through the first electron filter. If they are produced by collisions with the filter, however, they will also have potential energy: if in the production process they are sent through the filter, their total energy is enough to also go through the second filter, which means they will reach the collector causing a reduction in the collected signal.

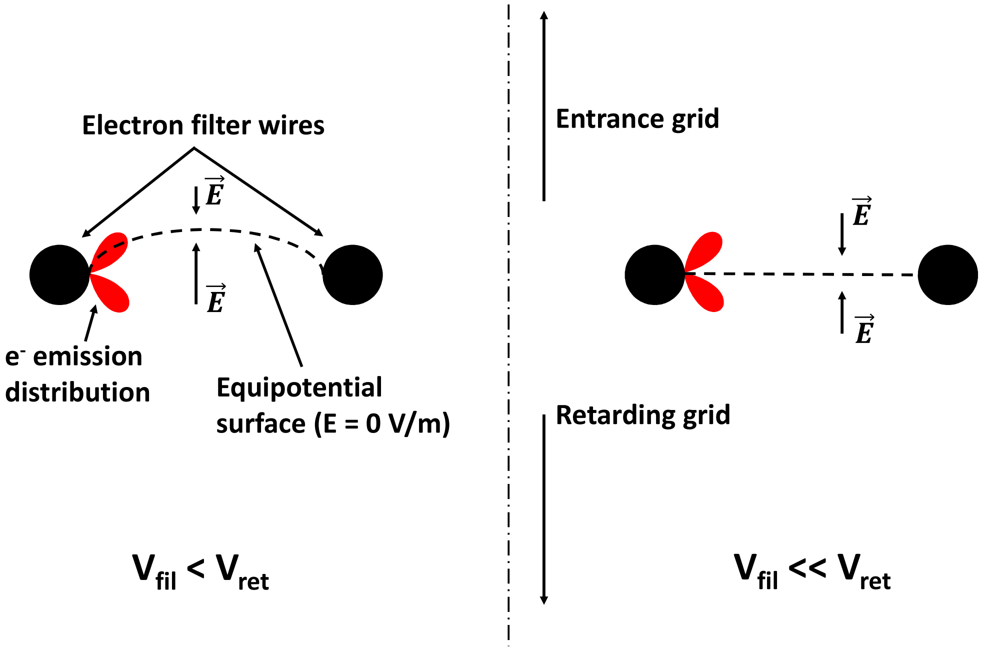

Figure 3.6: Electron emission due to ion collision with the electron filter.

This collision is also affected by an electrostatic lens effect that depends on the potential of the retarding grid, as seen in Fig. 3.6. During a measurement the potential of the entrance V_{ent} and the potential of the filters V_{fil} are kept constant with $V_{ent} > V_{fil}$, which means the electric field between these two grids $E_{1,2}$ is constant; the potential of the retarding grid V_{ret} is changed instead, thus changing $E_{2,3}$. When $V_{ret} > V_{ent}$ then $|E_{1,2}| < |E_{2,3}|$, which means equipotential surfaces at the grid will protrude from section 2-3 to section 1-2. When V_{fil} is comparable to the values in which V_{ret} ranges, the electrostatic lens effect is more evident and causes more electrons to be sent towards the collector. Due to the small size of the holes and wires of the grids, this lens effect is limited and higher values of V_{ret} do not yield more electrons. On other hand, when V_{fil} is much lower than V_{ret} the electrostatic lens effect is negligible and less electrons are sent towards the collector.

Overall, this emission of secondary electrons affected by V_{fil} causes a shift in current towards more negative values.

3.2 Design and construction

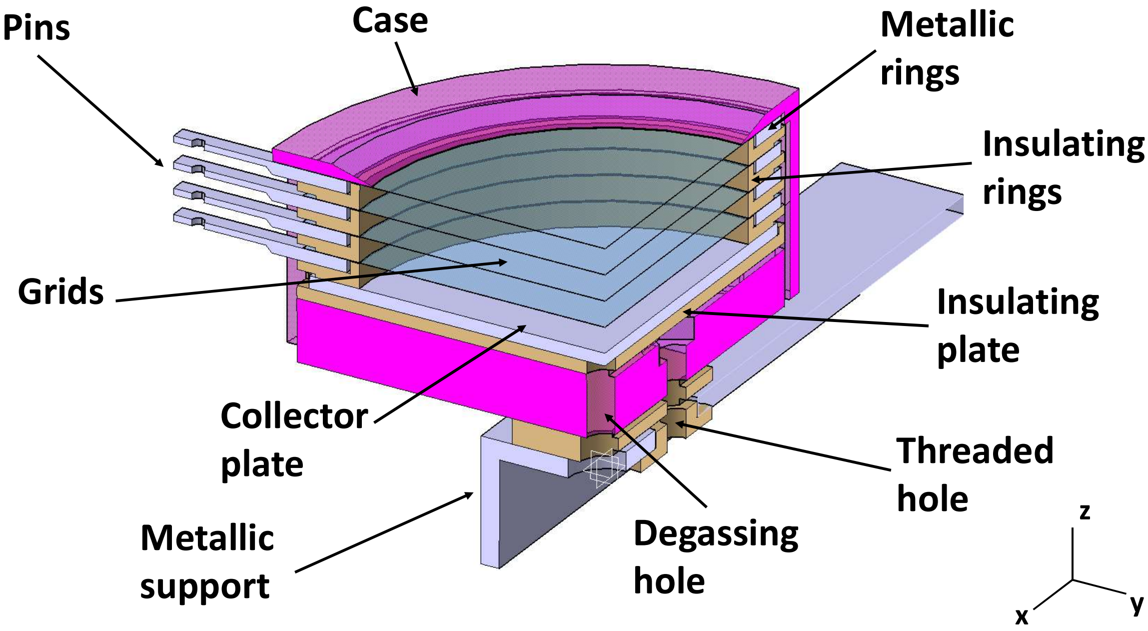

Figure 3.7: Double cross section of the analyzer along the planes xz and yz.

The final design of the analyzer is that of a metallic stainless steel cylindrical case with 10.4 cm in diameter, with an inner opening 8 cm in diameter. The four grids are welded on stainless steel rings that fit into the case and have an inner opening 8 cm in diameter; each ring is separated from the adjacent ones by insulating rings made of PEEK (total distance between grids is 4 mm), and apart from the one with the entrance grid, all other rings do not come into contact with the case. The pins seen on the left of Fig. 3.7 are part of the metallic rings and are needed to set the electric potential of each grid and to connect the analyzer to the acquisition circuit. The collector is a 2 mm thick stainless steel plate; below the collector is another insulating plate and then the metallic lid that closes the analyzer. The central hole at the bottom and the small open volumes between the rings allow for easier degassing when the analyzer is put into vacuum. The threaded hole is used to fix the analyzer to the support.

3.2.1 Materials used

The following materials have been chosen to build the analyzer:

- Stainless steel (AISI 304L, AISI 316L) for the case, the rings, the collector and the grids: it is conductive and can withstand the temperatures reached by the plasma;

- PEEK (polyether ether ketone) for the insulating rings and the insulating plate at the bottom: it can withstand up to 200 °C (it does not directly face the plasma) and is not conductive;

- Mylar (biaxially oriented polyethylene terephthalate) films and Kapton tape to cover and insulate the connections between the analyzer and the acquisition circuit: they are already suitable for use in vacuum.

3.2.2 Construction

After procuring three different types of meshes, for the test of their influence in the measurement, the analyzer was built by the workshop inside the Consorzio RFX facility in Padova (Fig. 3.8)

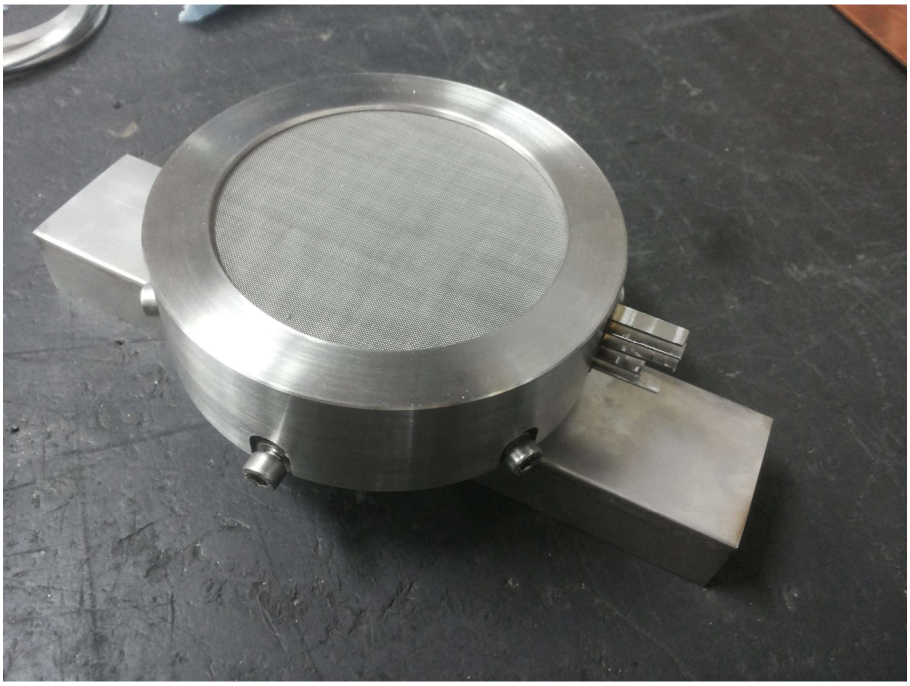

Figure 3.8: Picture of the energy analyzer.

Before being used in vacuum, the pieces of the analyzer need to be cleaned and made compatible with high vacuum: aluminum pieces were washed with acetone and ultrasound, PEEK pieces with acetone only.

3.2.3 Acquisition circuit

The analyzer needs to be connected to several power supplies in order to work properly, and the collected current also needs to be measured.
When inside vacuum, the signal travels through coaxial cables (one for each of the four grids plus one for the collector) in order to avoid interference from the plasma. The metallic shield of the cable is connected to the metallic chamber that encloses the vacuum, which is grounded, while the central core carrying the signal is connected to a 15 pin connector. Outside the chamber, the signal is then carried by a twisted pair still in order to avoid interferences. A simple schematic is shown in Fig. 3.9.

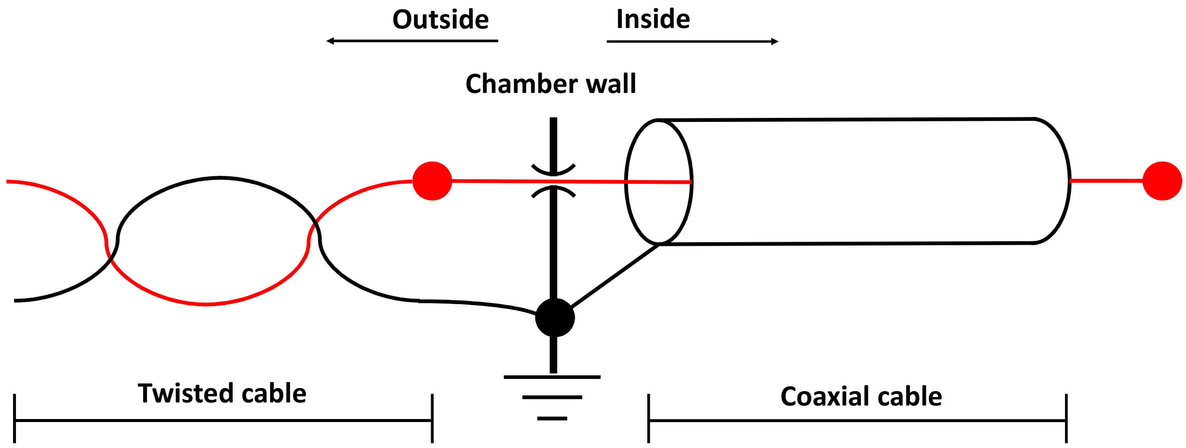

Figure 3.9: Pin connection scheme

The twisted pair then reaches an acquisition circuit(Fig. 3.10 and Fig. 3.11).

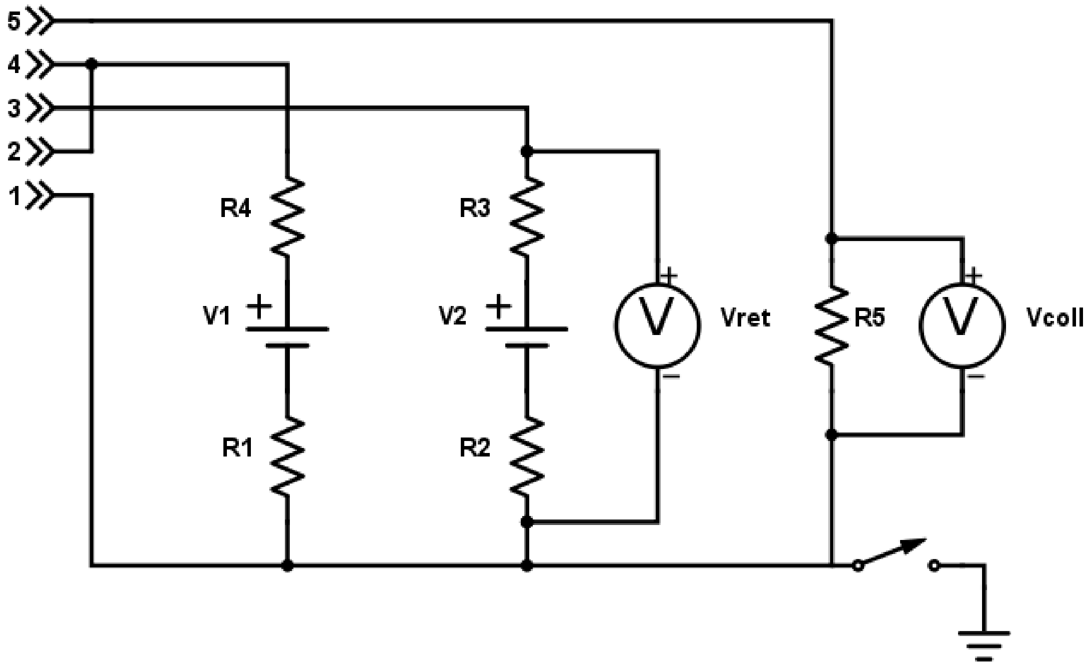

Figure 3.10: Acquisition circuit for the energy analyzer. The grids are numbered in the same order as in Fig. 3.1. Power supply V_1 gives negative potential to the electron filters, while V_2 is used to filter the ions based on their energy (The actual potential is measured through V_{ret}). The switch allows the entrance to either be grounded or left at floating potential. Collected current is measured with a voltmeter on R_5 ($I_{coll} = V_{coll}/R_5$).

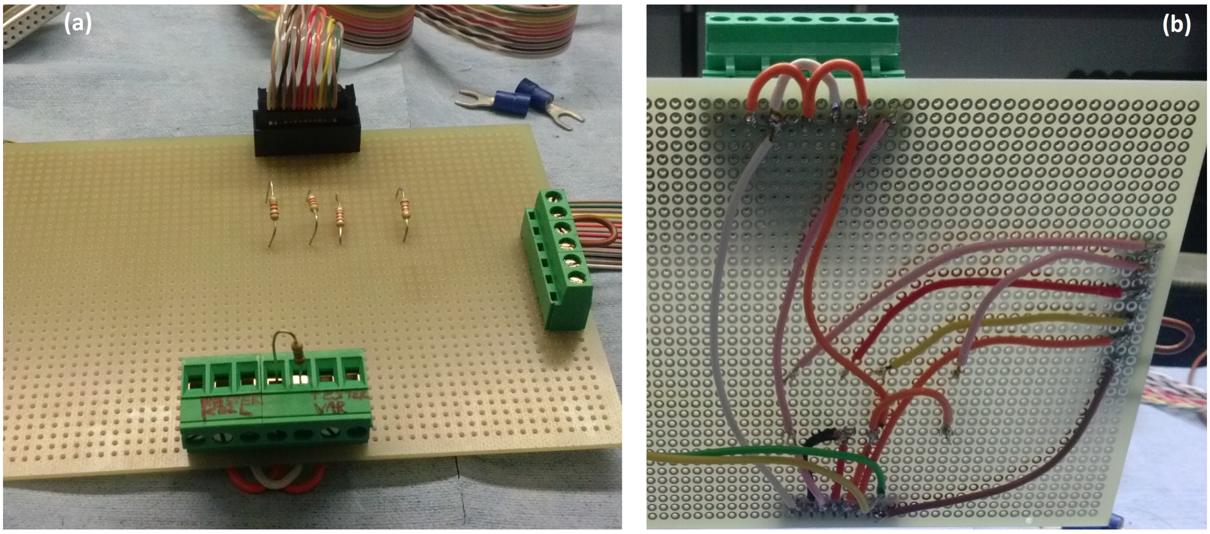

Figure 3.11: Pictures of the acquisition circuit. (a) Top view. (b) Bottom view

A second yet different acquisition circuit was also built: this allows the analyzer to be used also as a Langmuir probe [11], with the option of using only the case plus the first grid or even the case plus all the grids as collection area:

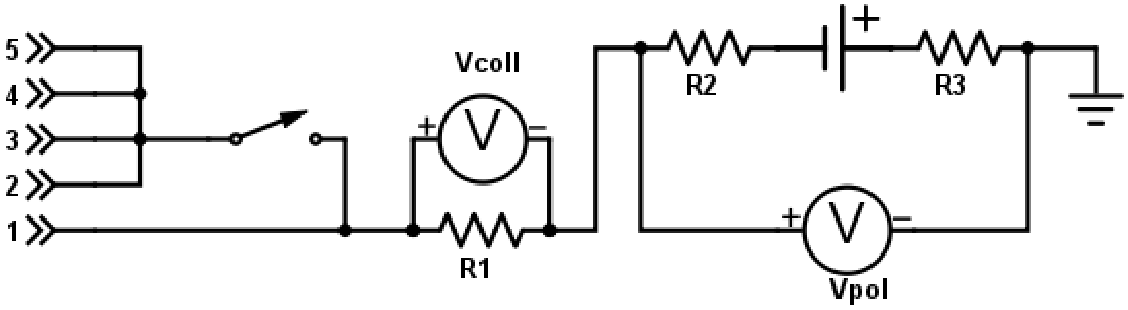

Figure 3.12: Acquisition circuit for Langmuir probe.

The resistances over which the collected current is measured (R_5 in Fig. 3.10 and R_1 in Fig. 3.12) are chosen each time so that the voltage drop over the resistance itself is readable but does not influence the measurement. Before and after each power supply is a 1.2 kΩ resistance to protect the power supply itself.

Chapter 4

Tests in Magnetron

After building the analyzer it's time to test it: the aim is to see if it works and what kind of signal it collects. The tests were done in a dc magnetron device at Consorzio RFX.

4.1 Experimental setup

The device (Fig. 4.1)consists in a cylindrical stainless steel vacuum chamber, 50 cm high and 40 cm wide. Inside it is a magnetron sputtering device source 10.16 cm in diameter with a stainless steel target. The source is provided with an array of permanent magnets located at the center and circularly at a radial distance of 40 mm from the source axis. The utilized power supply is a dc type, the maximum output is 1.5 kW. The gas used during the measurements was Argon [12].

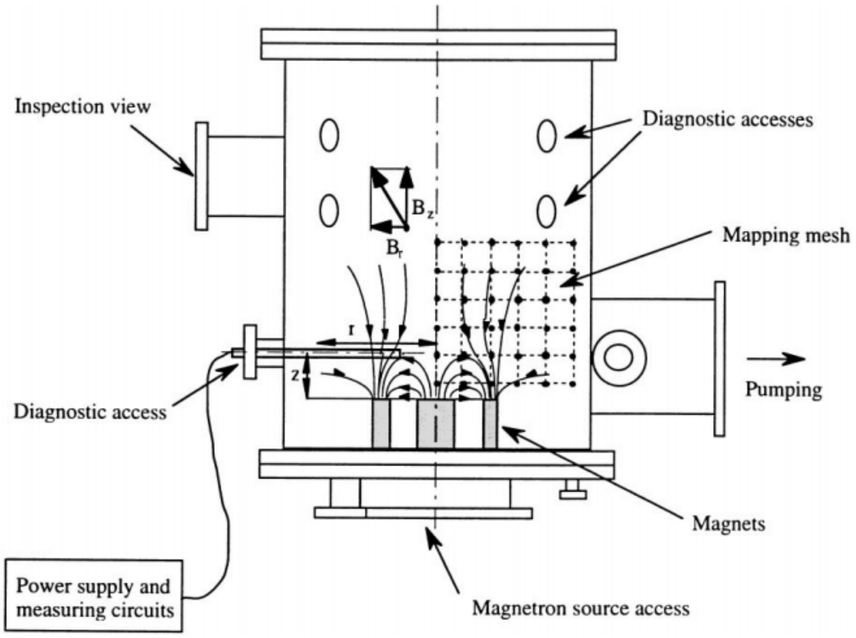

Figure 4.1: Magnetron device layout. The points in the mesh are only qualitatively indicated [12].

The energy analyzer is located on top of a stand facing towards the target (Fig. 4.2), with its axis coincident with the camber axis. The distance between the target and the analyzer is 16 cm. In this first assembly, all grids had transparency $\gamma = 35.6\%$

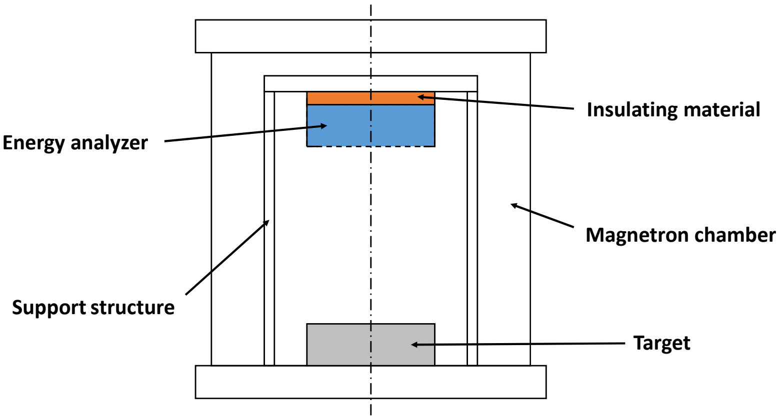

Figure 4.2: Location of the energy analyzer inside the chamber

4.2 Langmuir probe measurement

As stated in the previous chapter, the analyzer can be used as a Langmuir probe by using the acquisition circuit in Fig. 3.12. Three measurements of this kind were made. Two were made with output power supply of the magnetron device set to 14 W and the pressure inside the chamber set to 1 Pa: in the first one the case and the entrance grid were used as collection area, connected to each other and to the acquisition circuit, whereas all the other grids and the collector were not connected to anything; in the second one the other grids and the collector were used too (connected to the case). For the third measurement the power output was set to 77 W and the case, all the grids and the collector were used as collection area.

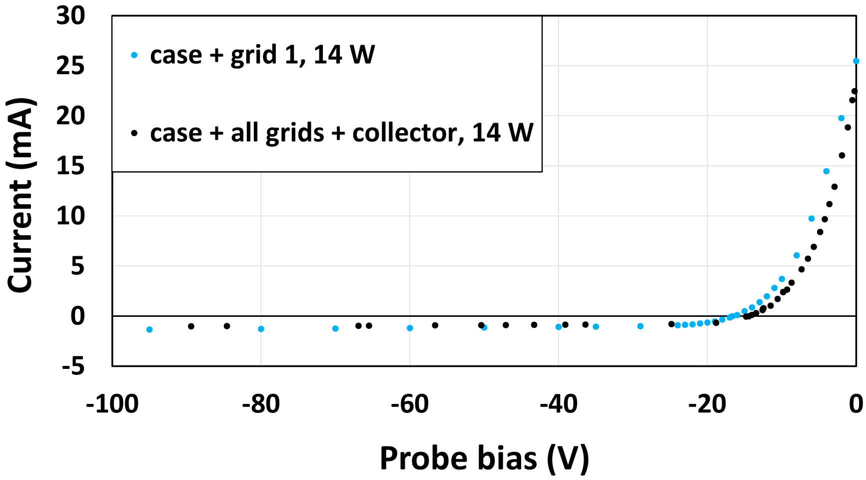

Figure 4.3: Current collected by the analyzer when used as a Langmuir probe (Pressure 1 Pa, power output 14 W).

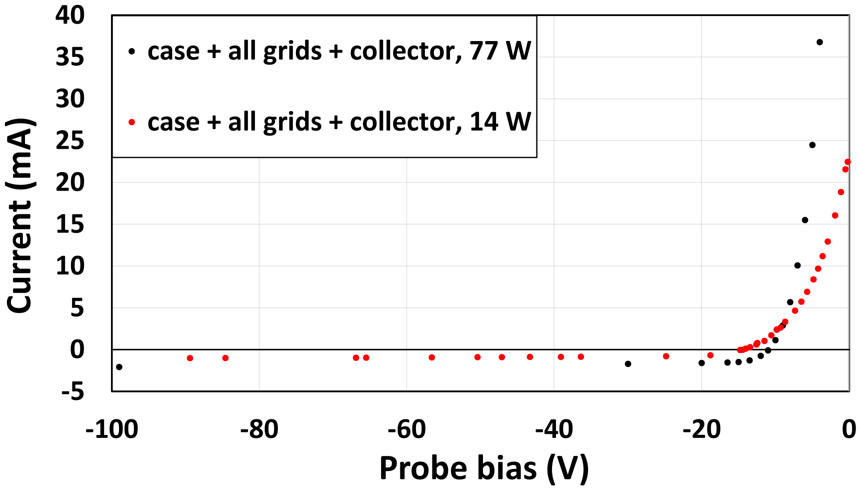

Figure 4.4: Current collected by the analyzer when used as a Langmuir probe (Pressure 1 Pa, case + all grids used).

4.2.1 Data comparison

When the power given to the magnetron device is kept constant and only the collection surface is changed (Fig. 4.3), the ion saturation current remains the same. The only things that change are the measured floating potential and the electron temperature: the

first increases while the second decreases.
When the power increases (Fig. 4.4), the floating potential is higher.
Since part of the collection surface is made of grids, some of the particles might go through without being collected. This effect can be seen in table 4.1: based on this, the measurements where all grids and the collector are used can be considered more reliable.

V_{case}	$V_{fil,1} - V_{case}$	$V_{ret} - V_{case}$	$V_{fil,2} - V_{case}$	$V_{coll} - V_{case}$
-14.6 V	-0.25 V	0.5 V	0.39 V	0.56 V

Table 4.1: Potential of each grid relative to the grid 1 (short circuited with the case), when the case is left floating and all other grids are only connected to grid 1 one at a time through the tester(pressure 1 Pa, power 14 W).

4.2.2 Data analysis

The total current collected by a Langmuir probe is

$$I = I_i^{MAX} \left(-1 + e^{-e(V_{bias}-V_{float})/k_B T_e}\right) \tag{4.1}$$

where I_i^{MAX} is the ion saturation current, V_{bias} is the potential given to the probe, V_{float} is the floating potential and T_e is the electron temperature.
Data is fitted by first subtracting the negative line and then fitting the exponential part: this allows to calculate T_e and V_{float}. With these, ion density n_i and plasma potential V_p are estimated as follows.
$I_{intersection}$ is calculated from the intersection of the negative line from the fit with the vertical line at $V_{bias} = V_{float}$. If one considers $A_{coll} = \pi R^2 + 2\pi R h = 1.46 \cdot 10^{-2}$ m^2 as the probe collection area, the current density is

$$j = \frac{I_{intersection}}{A_{coll}} \tag{4.2}$$

and the ion numeric density is

$$n_i = \frac{j}{0.6\, e\, \sqrt{k_b T_e / m}} \tag{4.3}$$

As for the plasma potential, it is calculated as

$$V_p = V_{float} + \frac{1}{2}\frac{k_B T_e}{e} \ln\left(\frac{m_i}{2\pi m e}\right) + \frac{1}{2}\frac{k_B T_e}{e} \tag{4.4}$$

An example of the fit is shown in Fig. 4.5, while numerical results are shown in Table 4.2.

Collection surface	Power supply (W)	V_{float} (V)	$k_B T_e$ (eV)	n_i (m^{-3})	V_p (V)
case + grid 1	14	-16.630	3.544	$2.406 \cdot 10^{14}$	1.739
case + all grids	14	-14.398	2.965	$2.109 \cdot 10^{14}$	0.968
case + all grids	77	-10.936	1.699	$5.628 \cdot 10^{14}$	-2.129

Table 4.2

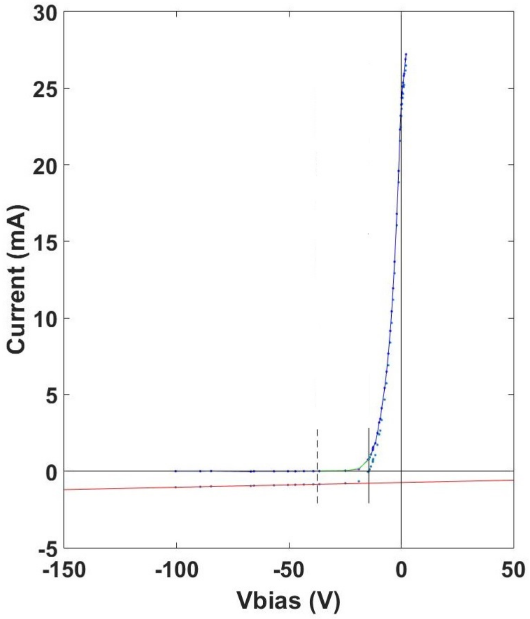

Figure 4.5: Fit of Langmuir measurement data (Pressure 1 Pa, power output 14 W, case + all grids used). The continuous line shows where V_{float} is, while the dashed line shows where points start to be counted for the exponential fit. The same analysis procedure is used for the other two datasets.

4.3 Energy analyzer measurement

By using the acquisition circuit in Fig. 3.10, the probe works as an energy analyzer. The output power supply of the magnetron device is set to 14 W and the pressure inside the chamber is set to 1 Pa.
Two groups of measurements are acquired: one with grid 1 grounded and one with grid 1 left floating. In each group three scans over V_{ret} were done, each time changing the value of V_{fil} (filters are connected to each other): -25V, -50 V and -100 V with grid 1 grounded, -10 V, -50 V, -100 V with grid 1 floating. These results are comparable to those reported in the original article on magnetron characterization [12].

4.3.1 Data comparison

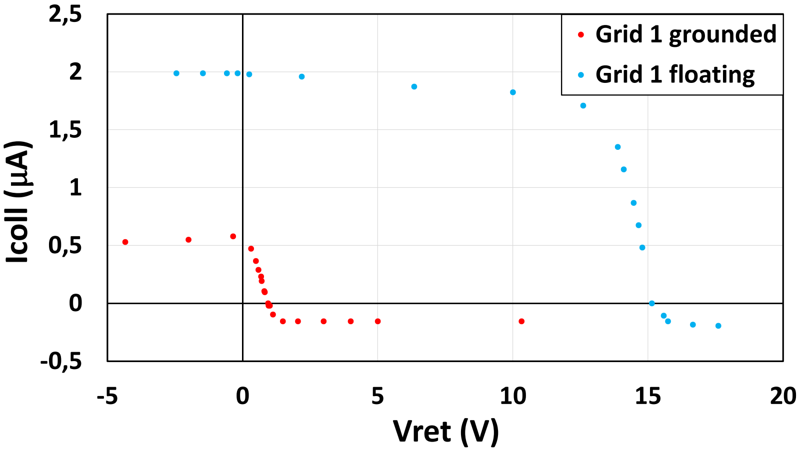

Figure 4.6: Comparison of collected current with grid 1 grounded and floating. ($V_{fil} = -100$ V, pressure 1 Pa, power output 14 W).

The two sets of measurements differ under several respects, as described in the following (Fig. 4.6).

Shift along V_{ret}

The value of V_{ret} where the curve rapidly starts decreasing is different in the two cases. When grid 1 is left floating its potential reaches -14.4 V, while when grid 1 is grounded its potential is 0 V: in the floating case the ions have additional 14.4 V and thus are more energetic when entering the analyzer, allowing them to go over higher values of V_{ret}.

Total current

While in the lower right parts of the plot both datasets show the same trend, the floating configuration shows a much higher ion saturation current on the left, reaching about four times as high as the other configuration. This is still related to the fact that $V_{case}^{GROUND} > V_{case}^{FLOAT}$, so when grid 1 is left floating more ions are being collected.

Ion saturation current

Both datasets show a smooth increase in the derivative value while reaching the maximum current value from the right hand side, but while the floating case shows saturation on the left of the peak, the ground case shows a sudden dip in current and only after that saturation is reached.

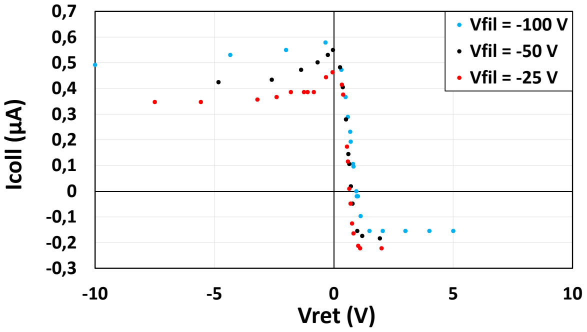

Figure 4.7: Results of measurements with grid 1 grounded (Pressure 1 Pa, power output 14 W).

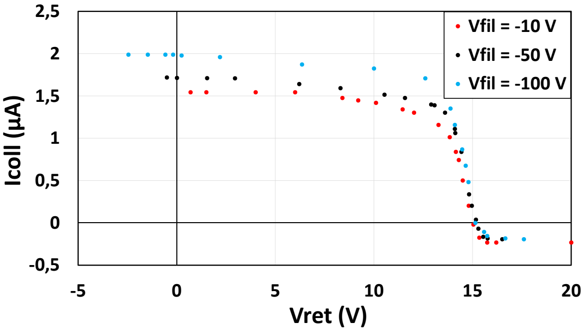

Figure 4.8: Results of measurements with grid 1 floating (Pressure 1 Pa, power output 14 W).

Lastly, there are also some common trends between the two sets of measurements regarding saturation current dependence on V_{fil} (Fig. 4.7 and Fig. 4.8).

Ion saturation current dependence on V_{fil}

Ion saturation current increases when $|V_{fil}|$ rises: this can be related to the observations made in chapter 3 when studying side wall loss.

Negative electron saturation current dependence on V_{fil}

The negative value of current saturation on the right hand side depends on V_{fil} and does not change with V_{ret}: as observed in chapter 3, this is caused by electrons produced at the first electron filter.

4.3.2 Data analysis

Gaussian fit

In order to estimate the energy spectrum of ions, a first basic analysis is made by interpolating the data with the following function:

$$F(V_{ret}) = \frac{K}{2}\left[1 + \text{erf}\left(\frac{-V_{ret} - A}{B\sqrt{2}}\right)\right] + C \tag{4.5}$$

where erf is the error function. This function has the shape of the CDF for the normal distribution, but stretched and moved along the y-axis and reflected relative to the y-axis. It is used simply because it can fit data very well and give a first rough estimate of average energy and temperature of ions.
These are the results (also seen in Fig. 4.9) calculated by analyzing the best dataset ($V_{fil} = -100$ V):

K	C	A	B
0.743 μA	0.15 μA	-0.67 V	0.33 V

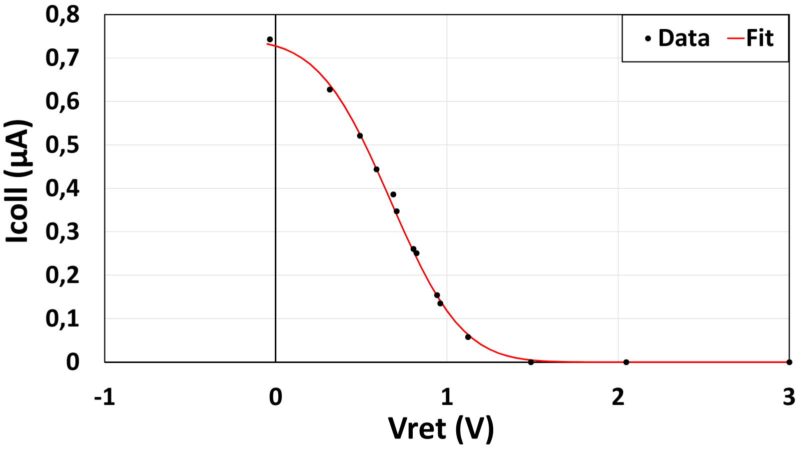

Figure 4.9: Gaussian fit ($V_{fil} = -100$ V, pressure 1 Pa, power output 14 W).

$-eA$ can be interpreted as the average ion energy and B as the speed with which the ion energy distribution lowers. The latter is caused by the fact that the ions are not created all in the same conditions: they are created in regions with different electric potential, and their velocity comes from a distribution.

First Gaussian moment fit

More in-depth analysis is made by making an educated guess on the velocity distribution of ions. The analyzer collects a flux of particles going towards the collector: the velocity distribution along the analyzer axis is expected to be the first moment of the Gaussian distribution:

$$f(v_z)d\vec{v} = K\, v_z\, e^{-v^2/2C} d\vec{v} \tag{4.6}$$

with $v_z \in (0, +\infty)$ and $v^2 = v_z^2 + v_\perp^2$.
The energy distribution then becomes

$$g(E) = Ae^{-(E-C)/B} \tag{4.7}$$

The dataset is then fit with the function

$$G(E) = \int_E^{+\infty} g(E)dE = A'e^{-(E-C)/B} \tag{4.8}$$

These are the results (also seen in Fig. 4.10) calculated by analyzing the best dataset ($V_{fil} = -100$ V):

A'	B	C
0.846 μA	0.265 eV	0.482 eV

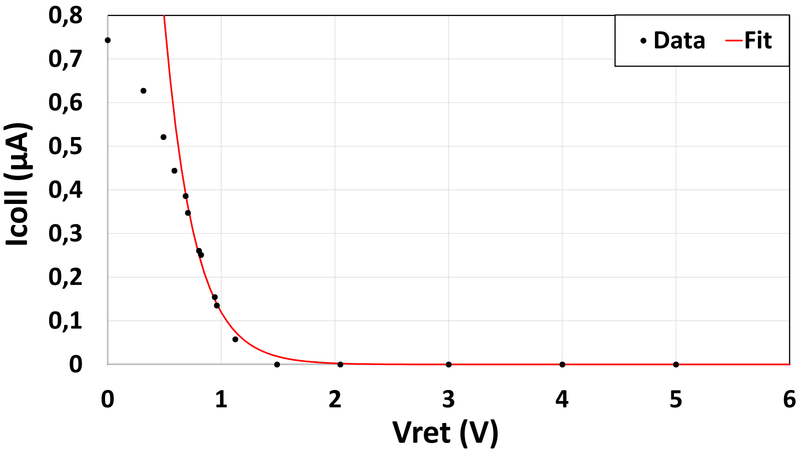

Figure 4.10: First Gaussian moment fit ($V_{fil} = -100$ V, pressure 1 Pa, power output 14 W).

B can be interpreted as the temperature of ions, while C is the minimum ion energy.
This fit does not cover the upper part of the current signal, where the second derivative changes from positive to negative: this feature is caused by collisions. Momentum transfer causes the energy components along different directions to mix, and in the case of $Ar^+ + Ar \rightarrow Ar^+ + Ar$ the mean free path is around 2 mm at pressure 1 Pa [13]: this means ions collide both in the sheath outside the analyzer and also inside the analyzer itself. Collisions on the outside make ions appear as if they were created with a lower overall energy (closer to the first grid and farther from the plasma core), while collisions on the

inside most of the times mean ions are lost, unless they are created in the small section where the potential is high enough to make them reach the collector (and only when $V_{ret} > 0$). Overall, this interaction has most impact when it happens on the outside, and it is the cause of the shape of the upper part of the signal.

These observations find further validation when studying electrons: by changing V_{fil} so that it is positive, ions can be kept out of the analyzer and only electrons are collected. The mean free path for momentum transfer for electrons is much bigger than the sizes of the sheath and of analyzer, so the effect described above should not be present. By looking at Fig. 4.11 one can see that this is exactly what happens: after mirroring the chart relative to the x and y axes, data clearly follows a decaying exponential trend and the same analysis used for ions can be applied to electrons. Results give minimum energy $E_e^{min} = 1.82$ eV and temperature $k_B T_e = 4.49$ eV.

Unfortunately during the measurements argon was available only as the process gas, but being able to explain every aspect of the collected signal and every unexpected trait has allowed a thorough understanding of how the analyzer works. Luckily the analyzer is to be used to analyze H_2^+ ions and the problems encountered with argon are not expected.

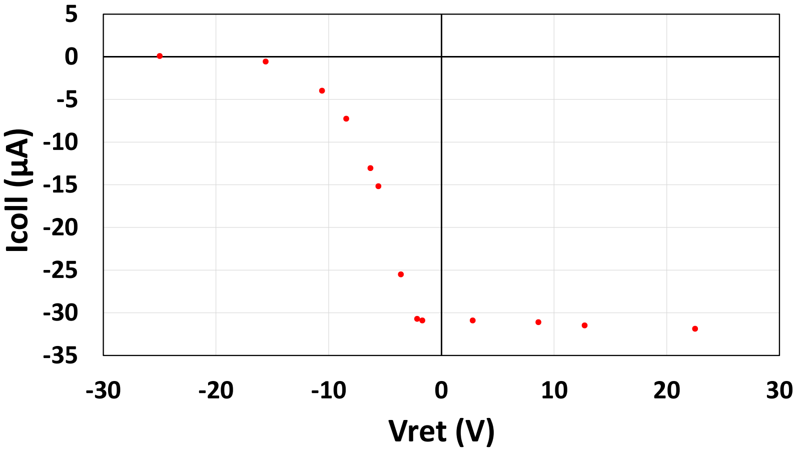

Figure 4.11: Collected current vs. V_{ret} ($V_{fil} = +50$ V, pressure 1 Pa, power output 14 W, grid 1 grounded).

4.3.3 Grid current

The current collected by the other grids has also been measured with grid 1 grounded. The retarding grid (Fig. 4.12) shows higher values of current for negative values of V_{ret}: the current quickly rises and then slowly reaches saturation. This is probably caused by the fact that, since $V_{ret} > V_{fil}$, as V_{ret} lowers it repels ions less, while electrons created at the first electron filter are attracted less; the saturation occurs due to the small size of the wires. The electron filters (which are connected to each other), on the other hand show lower values of ion current for negative values of V_{ret} (Fig. 4.13). By comparing both currents (Fig. 4.14) one can see that their sum is constant: this suggests that when

$V_{ret} < 0$ ions collide more with the retarding grid and less with the electron filters.

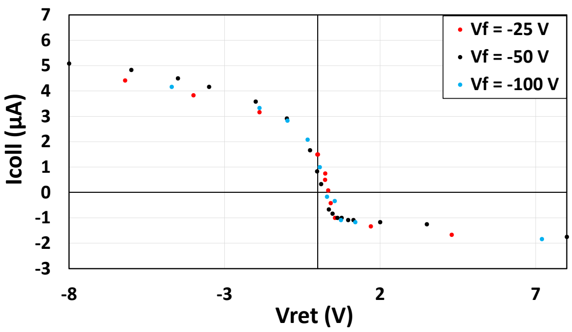

Figure 4.12: Current collected by the retarding grid (Pressure 1 Pa, power output 14 W, grid 1 grounded).

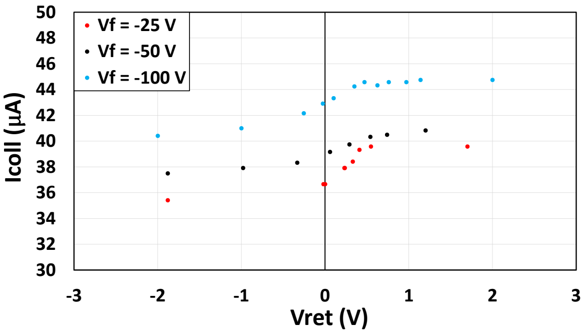

Figure 4.13: Total current collected by the electron filters (Pressure 1 Pa, power output 14 W, grid 1 grounded).

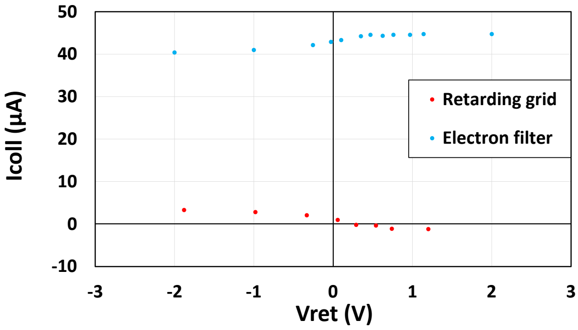

Figure 4.14: Comparison between electron filter and retarding grid ($V_{fil} = -100$ V, pressure 1 Pa, power output 14 W, grid 1 grounded).

4.4 Magnetron characterization

In order to complete an in-depth study of the plasma inside the magnetron device, additional scans with both the Langmuir probe configuration and the energy analyzer configuration have been made while changing the power output or the pressure inside the chamber.

Power scan

Saturation current values are measured with the energy analyzer configuration. Fig. 4.15 shows that the ion saturation current slightly increases until 16 W are reached and then starts rapidly decreasing for higher values of the power output, whereas the absolute value of negative electron current always increases.

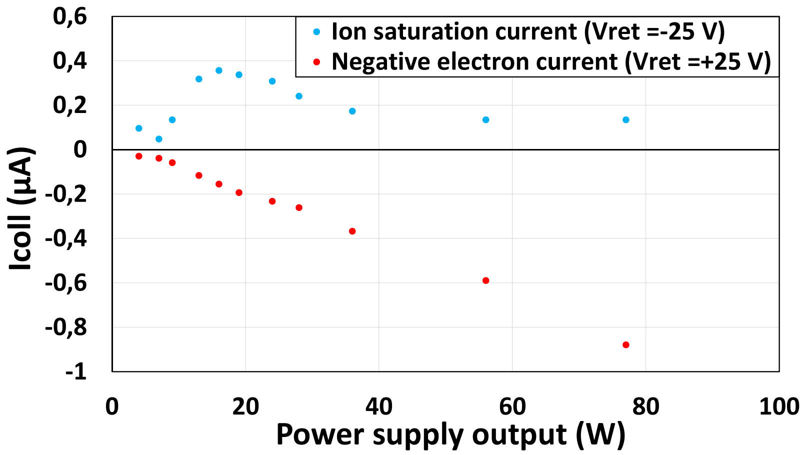

Figure 4.15: Ion saturation current and negative electron current vs. power output, measured with energy analyzer configuration ($V_{fil} = -100$ V, pressure 1 Pa, grid 1 grounded).

Pressure scan

Using the Langmuir probe configuration it is possible to measure the floating potential, which increases for higher values of pressure inside the chamber (Fig. 4.16).

When the energy analyzer configuration is used instead, ion saturation current is measured. Fig. 4.17 shows that total current decreases when the pressure inside the chamber increases. A complete scan over V_{ret} is made at three different values of pressure, as seen in Fig. 4.18.
As stated before, ion saturation current increases when pressure decreases. On the right hand side of the plot, however, the negative saturation current remains the same.
Lastly, one can see that the lower the pressure the higher the value of V_{ret} where negative saturation starts: this means that average ion energy is higher when the pressure is lower.

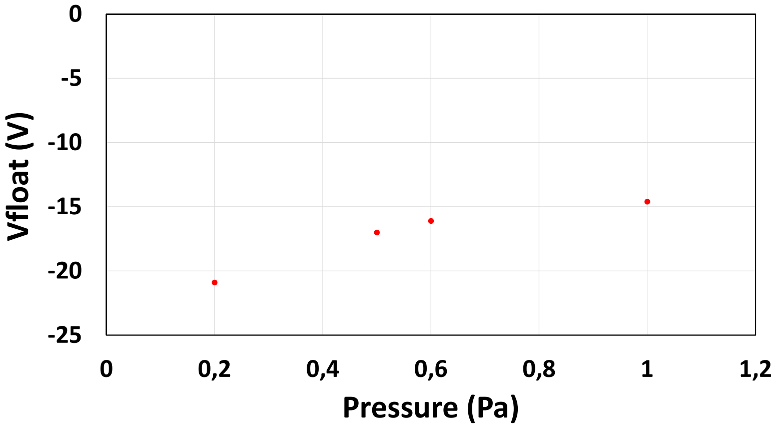

Figure 4.16: V_{float} vs. pressure. ($V_{fil} = -100$ V, $V_{ret} = -25$ V, power output 14 W, grid 1 grounded).

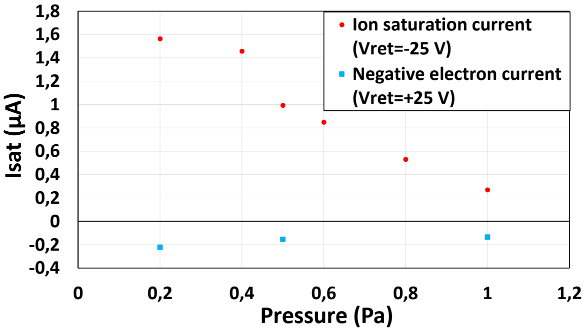

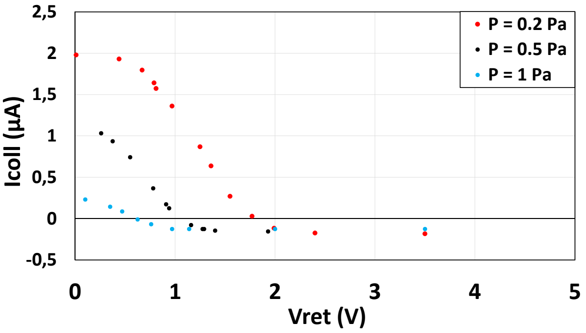

Figure 4.17: Ion saturation current and negative electron current vs. pressure. ($V_{fil} =$ -100 V, $V_{ret} = -25$ V, power output 14 W, grid 1 grounded).

Figure 4.18: Comparison of three scans at different pressure values ($V_{fil} = -100$ V, power output 14 W, grid 1 grounded).

Conclusion

All the results of data analysis are summarized in table 4.3.

		Langmuir Probe		**Energy analyzer**			
p (Pa)	P (W)	V_p (V)	k_BT_e (eV)	E_i^{min} (eV)	k_BT_i (eV)	E_e^{min} (eV)	k_BT_e (eV)
1	14	0.968	2.965	0.482	0.265	1.82	4.49
1	77	-2.129	1.699	0.175	0.409	–	–
0.5	14	–	–	0.624	0.395	–	–
0.2	14	–	–	1.1178	0.609	–	–

Table 4.3: Langmuir probe values are taken from measurements where all grids are used. Energy analyzer values for ions are taken from analysis with first Gaussian moment fit, $V_{fil} = -100$ V and grid 1 grounded; values for electrons are taken the same way but with $V_{fil} = +50$ V.

Chapter 5

Analysis of space charge compensation with a numerical simulation

After construction and tests, the analyzer is operational and will be used to study space charge compensation in negative ion beams located at the Consorzio RFX facility in Padova and at the NIFS facility in Toki, Japan.
In order to better understand the measurements that will be made, an accurate model that describes space charge compensation is needed. Due to difficulties involved in finding an exact solution to the partial differential equations associated to the system, a numerical approach has been chosen. This resulted in the development of a simulation code written with C++ and based on the particle-in-cell method (PIC) [14].

5.1 Particle-in-cell

This technique is commonly used to solve problems that are based on partial differential equations.
Particles are tracked in a continuous phase space, while quantities such as charge density or electric potential are calculated on the nodes of a mesh: a "cell" is a portion of the phase space delimited by two or more nodes (depending on chosen geometry). At any moment, each particle is confined inside a cell and gives its weighted contribution distributed over all adjacent nodes.
The main characteristics of the simulation are explained here in section 5.1, while section 5.2 explains the algorithm used.

Macroparticles

Each particle is actually a macroparticle that represents a group of individual particles: this allows the algorithm to converge much more quickly, but the total number of macroparticles is still high so that it is possible to have a meaningful statistics.

Collisionless plasma

The simulated group of particles is collisionless, but still gives meaningful results in a low pressure environment, where the mean free path is larger than the average distance traveled by the particles.

Phase space and mesh

The phase space where particles move is 2D with cartesian geometry: two independent directions, one parallel to the beam axis (z) and one perpendicular (x). It is to be noted that the mesh is only applied to the x axis: the simulation considers a uniform region 1 m long along z. Therefore, electric potential, charge density and particle generation do not depend on z coordinate and the only use for this direction is to remove particles that, after traveling for 1 m along this axis, have not yet reached the outer border of the x region. The inner border of the x region ($x = 0$) represents the beam center, while the outer border ($x = L$) represents the external grid of the analyzer. The distance between nodes Δx is chosen to be around half the expected Debye length: this way a good spatial resolution is achieved while still keeping the execution time of the simulation low.

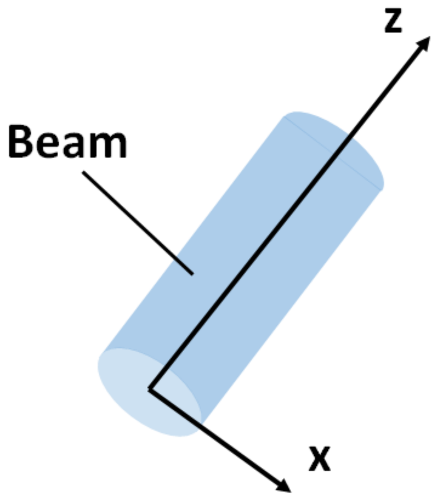

Time step

Time step of the simulation Δt is chosen so as to be around one tenth of $\tau_{pe} = 1/2\pi\omega_{pe}$: this way it is possible to solve plasma oscillations. This choice also assures that particles are not able to travel for more than one cell at each time step.

5.2 Algorithm

The steps followed by the simulation are shown in Fig. 5.1

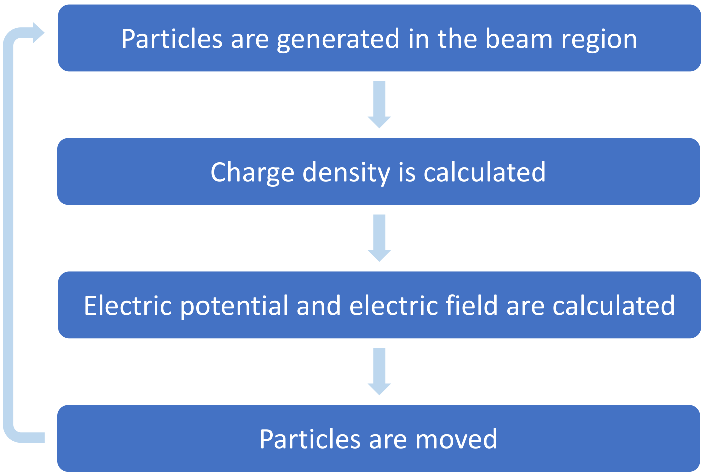

Figure 5.1: Simulation steps

Particle generation

The beam is modeled with density profile seen in (2.22) where $r = x$. Two source terms are calculated: one for ionization, which gives a pair of a H_2^+ ion and an electron, and one for electron stripping. Each source term is then obtained by integrating (2.9) over the volume of a beam that is 1 m long along z, and then divided by particle weight in order to take macroparticles into account. Effective cross section is used.
Each particle is then generated with a random position inside the beam (sampled from beam density profile) and given charge, mass, weight and initial velocity components v_x and v_z sampled from a distribution [5].
An example is displayed below, showcasing H_2^+ generation.

```
void Particle::startionizedion(double region){ \\create h2+
  vx = velfromnormal(T, h2mass);  //velfromnormal (T, m) samples
  vz = velfromnormal(T, h2mass);  //velocity from normal distribution
  double u, v, f;                 //with temperature T and mass m
  do{
    u = rand() / (1. + RAND_MAX);   //position sampling through
    v = rand() / (1. + RAND_MAX);   //rejection method
```

```
    u = u*region;
    v = v * 1.5 / region;
    f = (1.5 / region)*(1. - (u / region)*(u / region));
  } while (v > f);
  posx = u;
  posz=0.0;
  charge = q;
  mass = h2mass;
  weight = _wei;
}
```

Charge density

As stated earlier, charge density can only be calculated on mesh nodes. However, particles can be found anywhere in phase space, so their charge must be distributed between the two adjacent nodes (the mesh is only applied to direction x). The quantity of charge each node gets depends on how far the particle is from that node: if a particle with charge q_{part} and weight w_{part} lies between nodes i and $i+1$, then the charge on each node is

$$q_{i+1} = q_{part} w_{part} \frac{x_{part} - x_i}{\Delta x} \tag{5.1}$$

$$q_i = q_{part} w_{part} \frac{x_{i+1} - x_{part}}{\Delta x} \tag{5.2}$$

The 1D volume of a cell is Δx (distance between two adjacent nodes), so charge density of node i is

$$\rho_i = \frac{q_i^{tot}}{\Delta x} \tag{5.3}$$

Electric potential and field

Once charge density is known in each node, electric potential can be obtained through Poisson's equation

$$\frac{d^2\phi(x)}{dx^2} = -\frac{\rho(x)}{\epsilon_0} \tag{5.4}$$

which can be treated numerically as a finite difference equation (FDE).
Jacobi iterative method is chosen to solve this equation: at iteration $n+1$, potential at node i is calculated as

$$\phi_i^{n+1} = \frac{1}{2}\left(\phi_{i+1}^n + \phi_{i-1}^n\right) + \frac{1}{2}\frac{\rho_i\,(\Delta x)^2}{\epsilon_0} \tag{5.5}$$

Iterations go on until the difference between the old and new solutions is lower than a fixed threshold. Dirichlet boundary conditions are chosen for the node at $x = L$, while Neumann boundary conditions are chosen for the node at $x = 0$.
Once ϕ has been obtained, electric field is calculated in each node as centered discrete derivative of ϕ:

$$E_i = -\frac{(\phi_{i+1} - \phi_{i-1})}{2\Delta x} \tag{5.6}$$

Particle trajectory

The last step consists in moving particles. This is done with leap-frog algorithm:

$$v_{n+1/2} = v_{n-1/2} + a_n \mathit{\Delta} t \tag{5.7}$$

$$x_{n+1} = x_n + v_{i+1/2} \mathit{\Delta} t \tag{5.8}$$

This algorithm is not self-starting. In order to maintain a global 2^{nd} order relative to $\mathit{\Delta} x$ and $\mathit{\Delta} t$, when a particle is created it is necessary to calculate $v_{1/2}$ as

$$v_{1/2} = v_0 + a_0 \mathit{\Delta} t \tag{5.9}$$

Acceleration along z is always zero, but acceleration along x needs to be calculated each time as

$$a_x = \frac{qE(x_{part})}{m} \tag{5.10}$$

Since electric field is known only at nodes, if a particle is between nodes i and $i+1$ the electric field at particle position is

$$E(x_{part}) = E_i \frac{x_{i+1} - x_{part}}{\mathit{\Delta} x} + E_{i+1} \frac{x_{part} - x_i}{\mathit{\Delta} x} \tag{5.11}$$

After particles are moved, their position is checked to see if they are still inside the simulation region:

- If $x_{part} < 0$ the particle has gone beyond the beam center. Since statistically another particle is expected to come from that side with the same properties, position and velocity along x are simply mirrored.

- If $x_{part} > L$ the particle has reached the analyzer, which is grounded, and no longer contributes to space charge. Therefore, the particle is destroyed by setting its weight to zero.

- If $z_{part} > 1$ m, the particle has traveled too far along the beam axis. Again, it no longer contributes to space charge and it is destroyed.

5.3 Results

The simulation was performed with two different sets of parameters, one to emulate NIO1 at Consorzio RFX in Padova and one to emulate the beam at NIFS in Toki.

NIO1 [2]

The beam is made of 9 beamlets arranged in a 3x3 square grid, with side 2.8 cm long. Since the simulated region contains only a half of the total beam, generation region is 2 cm wide.
The analyzer is located 10 cm away from the beam center and 50 cm away from the acceleration grid.
Parameters of the simulation are: pressure 0.165 Pa, beam energy 5 keV, current 0.6 mA. Results of the simulation can be seen in Fig. 5.2 and 5.3.

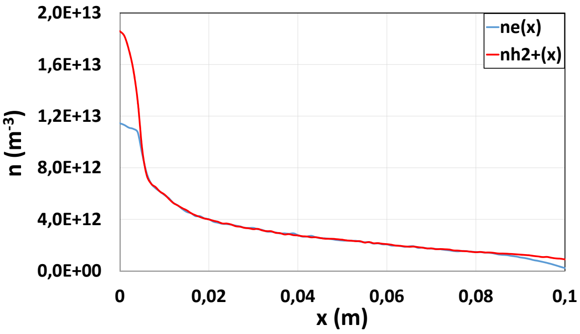

Figure 5.2: Ion and electron density vs. distance from the beam center.

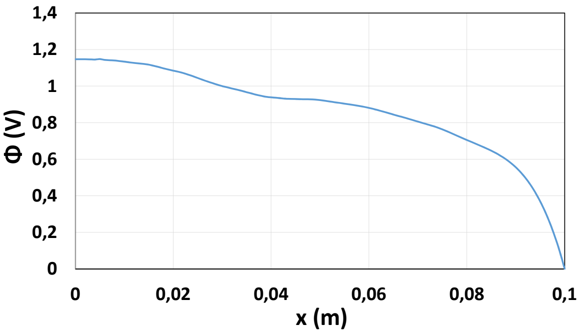

Figure 5.3: Electric potential vs. distance from the beam center.

The value of the potential inside the beam region is due to space charge compensation, and it is what should be measured with the analyzer.
It is to be noted that due to high pressure, collisions of ions with background gas are not negligible in the real environment. These collisions would keep ions from moving away from the beam too quickly: this means the value of the potential inside the beam region is an underestimate of what it would be in reality.

NIFS [8]

The beam is made of 30 beamlets arranged in a 5x6 rectangle, 8x10 cm^2: generation region is 5 cm wide.
The analyzer is located 13 cm away from the beam center and 1 m away from the acceleration grid.
Parameters of the simulation are: pressure 0.003 Pa, beam energy 60 keV, current 0.25 mA. Results of the simulation can be seen in Fig. 5.4 and Fig.5.5.

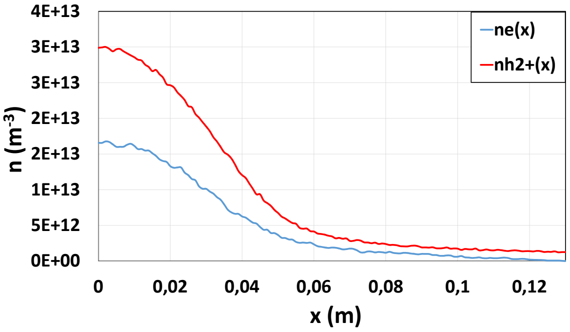

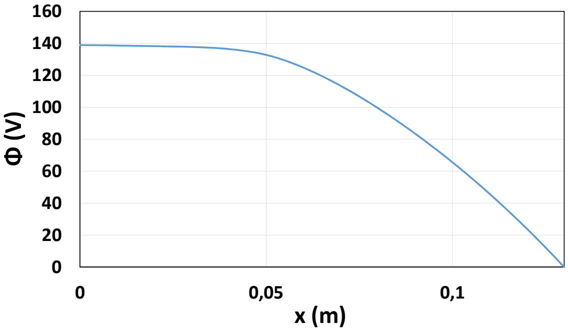

Figure 5.4: Ion and electron density vs. distance from the beam center.

Figure 5.5: Electric potential vs. distance from the beam center.

This time the low pressure of background gas means that collisions are negligible, therefore the electric potential in the beam region can be considered comparable to its real value.

Chapter 6

Conclusion

A deep understanding of space charge compensation is fundamental when studying negative ion beam transport: this phenomenon keeps the beam collimated and allows for transport over long distances.

Previous studies on NIO1 have highlighted the necessity for experimental measurements to further study space charge compensation. This requires an appropriate diagnostic: a retarding field energy analyzer was chosen.

The first step of the project was to understand the requirements of the analyzer, which are strictly related to the working environment. To do so, the interaction of beam particles with background gas was studied and results were used to create a numerical simulation: this allowed to estimate what the analyzer would measure in NIO1 and in the negative ion source at NIFS. After gathering this information, design was started and both an analyzer and a simple acquisition circuit were built.

After construction, tests in a magnetron device were made: unfortunately only argon gas was available, which caused some anomalies to appear in measurements due to its high collisionality. However, these anomalies were isolated and possible explanations for them were found, which allowed to verify the correct operation of the analyzer; these explanations are to be demonstrated in future tests with different conditions (e.g. different gas). In the end, finding these problems now might even be advantageous: if they will occur in future usage of the analyzer, their cause will already be known and they can be easily taken care of.

Considering that this is the first time an energy analyzer is developed at Consorzio RFX to operate in such a peculiar environment and in low density plasmas, the whole process covered by this thesis can be considered an original work, that will allow the institute to start experimental studies of the fundamental processes involving negative ion beam transport and beam plasma formation. The next step has already started at the moment of writing: an automatic acquisition circuit along with its control software were prepared, and the diagnostic is to be mounted inside the NIFS beam in Japan. After this first experimental phase it will come back to Consorzio RFX and will be mounted inside NIO1. After extensive operation in NIO1, a similar system might be designed and used to study space charge compensation in the negative ion source SPIDER at the Consorzio RFX facility, which will be operational in 2017.

On a personal level, working on this thesis has been an amazing experience. For the first time I have been able to thoroughly follow the process behind a new experiment: from the development of a model to explain a phenomenon, to the creation of a diagnostic to measure its properties and the testing of such diagnostic.
Being able to actively participate in this process and give my very own contribution, along with knowing that my work will actually be used to advance the research in nuclear fusion, has been truly rewarding and has enriched me as a future physicist and as a person.

Bibliography

[1] M. Cavenago *et al.*, "Development of small multiaperture negative ion beam sources and related simulation tools," *AIP Conf. Proc. 1097, 149*, 2008.

[2] M. Cavenago *et al.*, "First experiments with the negative ion source NIO1," *Rev. Sci. Instrum. 87, 02B320*, 2015.

[3] J. Lettry *et al.*, "Linac4 H^- ion sources," *Rev. Sci. Instrum. 87, 02B139*, 2015.

[4] M. Muramatsu and A. Kitagawa, "A review of ion sources for medical accelerators," *Rev. Sci. Instrum. 83, 02B909*, 2011.

[5] E. Sartori *et al.*, "Simulation of space charge compensation in a multibeamlet negative ion beam," *Rev. Sci. Instrum. 87, 02B917*, 2015.

[6] P. K. Roy *et al.*, "Electron-beam diagnostic for space-charge measurement of an ion beam," *Rev. Sci. Instrum. 76, 023301*, 2005.

[7] C. Ullmann *et al.*, "Investigation of ion beam space charge compensation with a 4-grid analyzer," *Rev. Sci. Instrum. 87, 02B938*, 2016.

[8] K. Tsumori *et al.*, "Negative ion production and beam extraction processes in a large ion source," *Rev. Sci. Instrum. 87, 02B936*, 2016.

[9] C. F. Barnett, "Atomic Data for Fusion," *ORNL-6086*, 1990.

[10] R. K. Janev and W. D. Langer, "Elementary Processes in Hydrogen-Helium Plasmas," *Springer*, 1987.

[11] N. Hershkowitz, "How Langmuir probes work," *Plasma Diagnostics*, 1989.

[12] M. Spolaore *et al.*, "Automatic langmuir probe measurement in a magnetron sputtering system," *Surface and Coatings Technology 116-119 1083-1088*, 1999.

[13] A. V. Phelps, "Cross Sections and Swarm Coefficients for Nitrogen Ions and Neutrals in N_2 and Argon Ions and Neutrals in Ar for Energies from 0.1 eV to 10 keV ," *J. Phys. Chem. Ref. Data 20, 557*, 1991.

[14] C. K. Birdsall and A. B. Langdon, "Plasma Physics via Computer Simulation," *Adam Hilger*, 1991.

Ringraziamenti

Voglio ringraziare di cuore tutte le persone che mi sono state accanto in questi mesi di lavoro.

Prima di tutto ringrazio i miei genitori, che si sono sempre presi cura di me con i loro consigli e le loro preoccupazioni.
Un ringrazimento speciale va poi a Sara, che riesce sempre a farmi sorridere e che mi ha aiutato a scacciare le preoccupazioni sulla consegna della tesi dicendomi "vedrai che non arrivi preso con le bombe".

Naturalmente un grande ringraziamento va a tutte le persone che ho conosciuto a RFX e che mi hanno regalato un'esperienza memorabile.
In particolare ringrazio il Dott. Gianluigi Serianni e il Dott. Emanuele Sartori che con pazienza hanno seguito il mio lavoro e hanno lasciato spazio al mio contributo, sempre interessati a sentire il mio parere e dandomi davvero la sensazione di poter portare un apporto concreto al loro progetto di ricerca. Un ringraziamento va anche al Dott. Pierluigi Veltri, che si è sempre dimostrato disponibile a darmi consigli anche quando era impegnato in altre cose e assieme ad Emanuele mi ha insegnato a saldare circuiti con lo stagno. Ovviamente ringrazio anche Vannino Cervaro, che ha costruito la sonda, e la Dott.ssa Monica Spolaore e il Dott. Roberto Cavazzana che mi hanno permesso di utilizzare il dispositivo magnetron del loro gruppo per fare i test. Infine, ringrazio il Dott. Vanni Antoni, che si è sempre mostrato entusiasta per questo progetto e si è pure fermato ad aiutarmi a fare alcune misure.
Senza tutti loro questa esperienza non sarebbe stata possibile e non mi sarei mai divertito così tanto.